Structure and thermal regime beneath the South Pole region, East Antarctica, from magnetotelluric measurements

Philip E. Wannamaker,[1] John A. Stodt,[1] Louise Pellerin,[1] Steven L. Olsen[2] and Darrell B. Hall[3]

[1]*University of Utah, Energy & Geoscience Institute,* 423 *Wakara Way, Suite* 300*, Salt Lake City,* UT 84108*, USA. E-mail: pewanna@egi.utah.edu*
[2]*RedRock Analog Design, Salt Lake City,* UT 84105*, USA*
[3]*University of Utah, Department of Geology and Geophysics, Salt Lake City,* UT 84112*, USA*

SUMMARY
Ten tensor magnetotelluric (MT) soundings have been acquired in a 54 km long profile across the South Pole area, East Antarctica. The MT transect was offset from the South Pole station ∼5 km and oriented 210 grid north, approximately normal to the Trans-Antarctic Mountains. Surveying around South Pole station was pursued for four main reasons. First, we sought to illuminate first-order structure and physico-chemical state (temperatures, fluids, melts) of the crust and upper mantle of this part of East Antarctica. Secondly, conditions around the South Pole differ from those of previous MT experience at central West Antarctica, so that the project would help to define MT surveying feasibility over the entire continent. Thirdly, the results would provide a crustal response baseline for possible long-term MT monitoring to deep upper mantle depths at the South Pole. Fourthly, because Antarctic logistics are difficult, support facilities at the South Pole enable relatively efficient survey procedures. In making the MT measurements, the high electrical contact impedance at the electrode-firn interface was overcome using a custom-design electrode pre-amplifier at the electrode with low output impedance to the remainder of the recording electronics. Non-plane-wave effects in the data were suppressed using a robust jackknife procedure that emphasized outlier removal from the vertical magnetic field records. Good quality data were obtained, but the rate of collection was hampered by low geomagnetic activity and wind-generated, electrostatic noise induced in the ice. Profile data were inverted using a 2-D algorithm that damps model departures from an *a priori* structure, in this case a smooth 1-D profile obtained from inversion of an integral of the TM mode impedance along the profile. Inverse models show clear evidence for a pronounced (∼1 km thickness), conductive section below the ice tentatively correlated with porous sediments of the Beacon Supergroup. Substantial variations in sedimentary conductance are inferred, which may translate into commensurate variations in sediment thickness. Low resistivities below ∼30 km suggest thermal activity in the lower crust and upper mantle, and mantle support for this region of elevated East Antarctica. This contrasts with resistivity structure imaged previously in central West Antarctica, where resistivity remains high into the upper mantle consistent with a fossil state of extensional activity there.

Key words: Antarctica, electrometer, magnetotellurics, thermal regime, South Pole.

INTRODUCTION

Approximately 95 per cent of Antarctica is covered with thick (1–3 km) ice, and so most crust and mantle structure must be deduced geophysically. Nevertheless, this major land mass is an essential but still poorly understood component of lithospheric plate reconstructions especially of the Pre-Cambrian and Early Paleozoic times (Dalziel 1997; Dalziel & Lawver 2001). Moreover, evidence is strong that Antarctica has been subject to Cenozoic plume activity

and represents an important location to study modification of previously stable cratonic lithosphere by plume processes, but which has resulted in only limited surface rifting.

Geophysical deductions must make use of only a handful of physical properties of the Earth, one of which is its electrical resistivity. The geophysical method that can provide images of resistivity to deep crustal or upper mantle depths is magnetotellurics (MT) (Vozoff 1991; Wannamaker & Hohmann 1991; Jones 1992, 1999; Wannamaker 2000). This physical property in turn can supply

information on primary structures (sedimentary distributions, lithologic contrasts, major fault offsets), geochemical fluxes (hydrothermal alteration, remobilized graphite and sulphides) and thermal regime (prograde or melt-exsolved fluids, crustal or upper mantle melts, mineral semi-conduction). While the technology to acquire good MT data in temperate zones is reasonably well understood, polar regions present special challenges.

For the MT method to be feasible throughout the Antarctic continent, one must be able to acquire high-quality electric field data over the highly resistive, interior ice sheets. Electrode contact resistances in near-surface ice (firn) may reach several Mohms (Shabtaie & Bentley 1995) requiring specialized electronics to acquire accurate electric field data. Using an in-house design, we acquired profiles of good-quality MT sites, first in central West Antarctica (CWA), and more recently across the region of the South Pole station, East Antarctica. The latter, upon which we report here, consist of 10 sites over a transect length of 54 km. Our measurements provide a new view of the geology and physical state below the South Pole area, and characterize important environmental variables pertinent to obtaining high-quality MT results in polar regions.

GEOLOGICAL SETTING

Antarctica is divided fundamentally into eastern and western portions separated by the continent-dissecting Trans-Antarctic Mountains (TAM) (Fig. 1). East Antarctica has been accepted as a stable cratonic block of Pre-Cambrian rocks, but more recently is thought to have been a component of a Late Proterozoic supercontinent Rodinia (e.g. Dalziel 1991, 1997; Borg & DePaolo 1994; Rodgers *et al.* 1995; Dalziel & Lawver 2001; Karlstrom *et al.* 2001). West Antarctica has been assembled to East Antarctica from accreted blocks and subduction-related plutonism since lower Paleozoic time (Storey & Alabaster 1991). Down-sagging but otherwise stable conditions in western East Antarctica from late Paleozoic through Jurassic time promoted deposition of the often thick (to 2.5 km) Beacon Supergroup of clastic rocks (Barrett 1991).

Convergent tectonics in West Antarctica through Triassic time gave way to extension associated with Gondwana breakup and subsequent events through the Cretaceous into the Cenozoic (Behrendt *et al.* 1991; Storey & Alabaster 1991; Cande *et al.* 2000; Dalziel & Lawver 2001). In West Antarctica, this multistage extension has been accompanied by episodic uplift and denudation of the TAM (Fitzgerald 1994; Fitzgerald & Stump 1997), by graben formation beneath the Ross Sea and exposed in Marie Byrd Land (Behrendt *et al.* 1991; Davey & Brancolini 1995), and by Middle to Late Cenozoic volcanics in Marie Byrd Land, Victoria Land, and the Horlick Mountains (LeMasurier & Rex 1991). Late Cenozoic extension is limited and correlation of the volcanism with plate tectonic events is difficult; it is thought to reflect presence of a mantle plume under the stationary Antarctic plate (Hole & LeMasurier
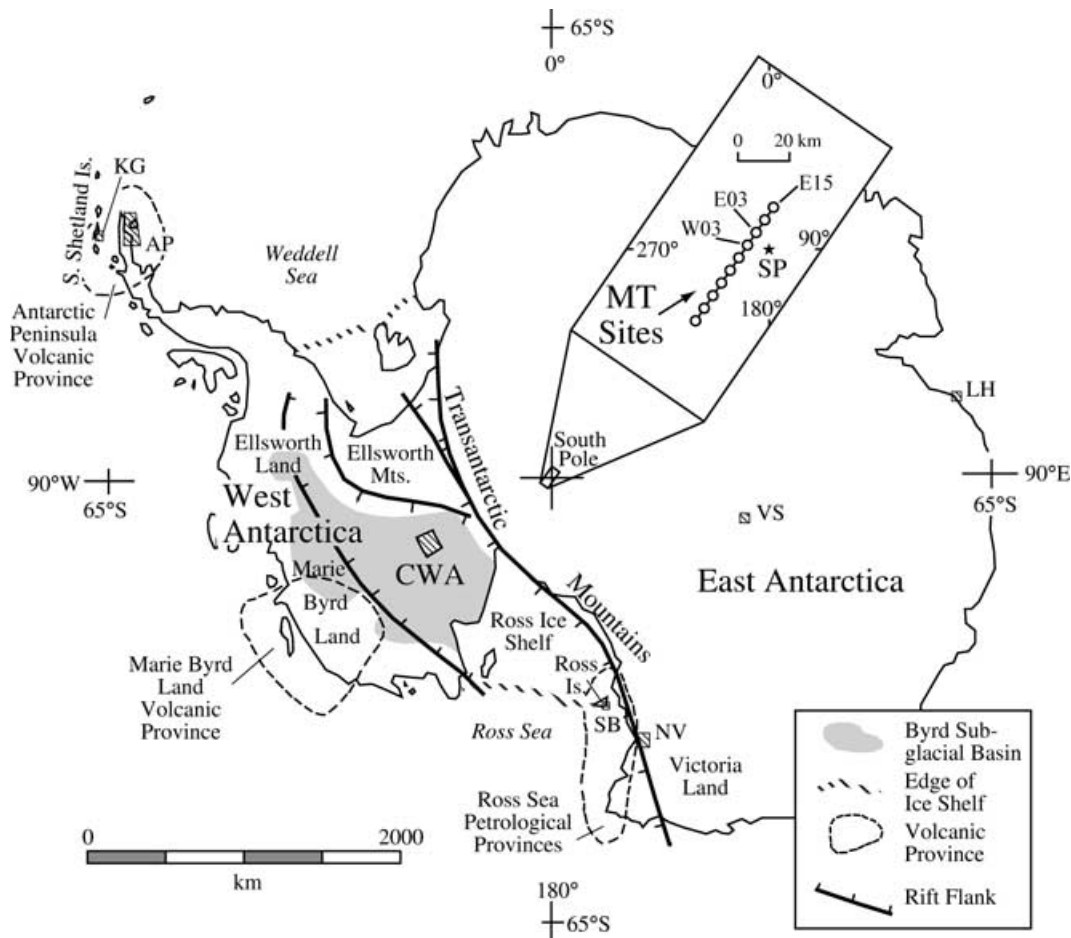

Figure 1. Field site map for MT at the South Pole station (SP). General location of earlier Central West Antarctica (CWA) experiment is shown also. Site spacing at both field areas is approximately 6 km. Grid north is up. Other regions where previous natural field MT experiments described in the text were attempted include King George Island (KG), Antarctica Peninsula (AP), Scott Base (SB), North Victoria Land (NV), Larsemann Hills (LH) and Vostok (VS). Sites discussed in the text are labelled in the inset in abbreviated form. Modified from LeMasurier & Rex (1991).

1994; LeMasurier & Landis 1996; Behrendt 1999; Dalziel & Lawver 2001).

GEOPHYSICAL INFERENCES

Crustal thickness of East Antarctica appears to average approximately 40 km based on seismic refraction profiles near its NE coast, and gravity interpretations region-wide, in contrast to 20–30 km for much of rifted West Antarctica (Bentley 1991; Behrendt 1999). Surface wave studies confirm separateness of East and West Antarctica, with the former showing more craton-like velocities on average, and with the highest lateral gradient in model velocities typically occurring below the South Pole itself (Bentley 1991; Roult *et al.* 1994; Danesi & Morelli 2000; Ritzwoller *et al.* 2001). Seismic refraction surveying measured no return energy at the South Pole (Bentley & Clough 1970), which may be taken at face value or could suggest that there is subcropping sedimentary section (Beacon Supergroup?) beneath the South Pole ice sheet of ~1 km thickness or more (Bentley 1973, 1991). Ice thickness at the South Pole is ~2800 m based on radar sounding (Jiracek 1967; Bentley 1991). Ice-stripped, rebounded basement elevations of East Antarctica are anomalously high (1–3 km) suggesting some kind of active tectonic support (Bentley 1991).

Seismicity throughout Antarctica is low, consistent with a slow-moving plate almost entirely surrounded by mid-ocean ridges, but with the west approximately 10 times more active than the east (Bentley 1991; Hole & LeMasurier 1994). Aeromagnetic and seismic refraction surveys suggest basaltic rocks are present along the base of the West Antarctica ice sheet (Byrd Subglacial Basin), comparable with outcrop and geophysical characteristics of Marie Byrd Land (Behrendt *et al.* 1991, 1994; Blankenship *et al.* 1993; Behrendt 1999) (Fig. 1). Recent aerogeophysical surveying (magnetics, gravity, radar, altimetry) with sparse ground geophysics (seismic refraction, MT discussed below) provide a picture for the Byrd Basin of localized Late Cenozoic volcanism along zones of weakness originating in the main Cretaceous rifting event and reactivated during recent plume uplift (Blankenship *et al.* 2001).

The character and scale of the geomorphology and tectonic style have lead some to compare West and East Antarctica with the extensional northern Basin and Range (Great Basin) and stable interior of the western US, with the TAM representing a regional rift shoulder similar to the Wasatch Range (Storey & Alabaster 1991; Rocholl *et al.* 1995). Important differences, however, include time of rifting, plate boundary forces, and magmatic petrogenesis (ten Brink *et al.* 1993; Hole & LeMasurier 1994; Humphreys & Dueker 1994; Sonder & Jones 1999). More recently, ten Brink *et al.* (1997) modelled gravity and seismic structure across the Ross Sea-TAM transition in southern Victoria Land in terms of flexural uplift, with an effective elastic thickness in this part of East Antarctica of ~80 km, which is thick compared with other uplifted but otherwise inactive terranes such as the Colorado Plateau (Lowry *et al.* 2000).

BRIEF INTRODUCTION TO MAGNETOTELLURICS

The MT method uses naturally occurring electromagnetic (EM) wavefields as sources for imaging the electrical resistivity structure of the Earth (Vozoff 1991). The incident EM waves usually are treated as planar in geometry and propagating vertically downward. In the conducting Earth, EM waves at typical frequencies of the method (<1000 Hz, for example) travel diffusively, such that high-frequency (short period) waves penetrate a relatively short distance while low-frequency (long period) waves can reach into the mantle. Special challenges to collecting good MT data over polar ice sheets include the very high contact impedance at the electrode-firn interface for the **E**-field measurement and possible violations of the planar EM wave assumption due to proximity to the polar electrojet (Mareschal 1986; Pirjola 1998; Jones & Spratt 2002).

The electric (**E**) and magnetic (**H**) vector fields scattered by buried structure and measured at the surface may have arbitrary polarization relative to the incident fields. This requires a tensor relationship between the measured fields as a function of frequency (or period T, its inverse) denoted for the horizontal components through

$$[\mathbf{E}] = [\mathbf{Z}][\mathbf{H}],$$

where $\mathbf{Z}$ is the 2×2 complex impedance. The individual impedance elements typically are transformed into an apparent resistivity (ρ_a) and an impedance phase (φ) for presentation and modelling. On a uniform half-space of resistivity ρ, $\rho_a = \rho$ and $\varphi = 45°$. For more complex structures, ρ_a versus T approximates a smoothed version of ρ versus distance below the measurement. The phase φ tends to be proportional to slope of ρ_a versus T, and thus is more reflective of spatial gradients in the subsurface resistivity. These primary data in turn are transformed to constrained resistivity models through the process of inversion, specified in the model construction section below.

Over 2-D structures where one of the measurement axes is parallel to geoelectric strike (x here by convention), the diagonal entries of $\mathbf{Z}$ are zero (Vozoff 1991). In this situation, the MT response separates into two independent modes. These are the transverse electric (TE) mode, where $E_x = Z_{xy}H_y$ and electric current flows parallel to strike (x-axis), and the transverse magnetic (TM) mode, where $E_y = Z_{yx}H_x$ and current flows perpendicular to strike (y-axis). Additionally, a 1×2 tensor $\mathbf{K}_z$ relates the vertical and horizontal magnetic fields through

$$[H_z] = [\mathbf{K}_z][\mathbf{H}].$$

For a 2-D Earth, $K_{zx} = 0$ and K_{zy} reflects cross-strike changes in current flowing along strike (TE mode).

PREVIOUS MT IN ANTARCTICA

Hessler & Jacobs (1966) recorded analogue, long period ($T > 1$ min) **E**-fields over glacial ice at Vostok with 200 m bipoles and copper screen electrodes buried in brine-soaked firn. Correlations were visible with simultaneous magnetic records, but large spike noise was common and no MT impedances were estimated. MT measurements were taken by Fournier (1994) on the Antarctic peninsula but electrical contact either was on exposed earth or sea ice of similar resistivity (1000 ohm m) and so not characteristic of the continental interior. This appears to have been the case as well in the surveys of Kong *et al.* (1993, 1994) on the Fildes peninsula of West Antarctica and near the Larsmann Hills of East Antarctica.

Good-quality MT data at relatively long periods (20–2000 s) were acquired by Beblo & Liebig (1990) over thin glacial ice cover in North Victoria Land. They used copper screens as electrodes over a 25 m bipole span and an electrometer of very high input impedance (10^{+12} ohm m). Signals in this longer period range are due to high-amplitude ionospheric micropulsations, but the lack of shorter period data makes it difficult to quantify resistivity of most of the crustal column. However, the authors did show that sounding results during both low- and high-activity times of the polar electrojet

were very similar, from which they concluded that non-plane-wave source effects were not a serious issue.

The first high-quality broad-band MT soundings over the thick interior ice sheet of Antarctica were obtained by Wannamaker *et al.* (1996) in CWA over Whitmore Mountains–Ross Embayment transitional crust (Blankenship *et al.* 2001) (Fig. 1). The primary technical difficulty of acquiring the **E**-field measurements on thick glacial ice was overcome using a custom electrometer system, discussed in Appendix A. A total of ten tensor soundings in the period range 0.01–500 s approximately were taken in a profile closely parallel to a seismic reflection line as part of the Antalith project (Clarke *et al.* 1997; Sen *et al.* 1998). 2-D, trial-and-error modelling of the data profile using the finite-element algorithm of Wannamaker *et al.* (1987) was carried out with ice thickness variation constrained according to seismic reflection results (Sen *et al.* 1998) and an average ice resistivity of 300 000 ohm m (Shabtaie & Bentley 1995).

In the model of Wannamaker *et al.* (1996), most of the subice section even into the upper mantle is resistive (>1000 ohm m), implying a dormant state of rifting at most (*cf.* Wannamaker *et al.* 1997). Our correlations are supported by the reversed refraction profiling at CWA which implies upper mantle P_n velocities of 8.0–8.1 km s^{-1} (Clarke *et al.* 1997). Mantle *S*-velocity structure of the West Antarctic Rift region is lower than the global average, but nearly indistinguishable from that of other dormant rift zones worldwide such as the western Mediterranean and the Sea of Japan (Ritzwoller *et al.* 2001). We concur with the earlier description of LeMasurier & Rex (1991) and Hole & LeMasurier (1994) that volcanic activity at present is restricted to occasional, narrow conduits ultimately fed from a deep plume source. These in turn are interpreted to be reactivation zones originating in the previous, mainly Cretaceous rift event (Blankenship *et al.* 2001). However, it is noted that the profile we acquired is 54 km in length and may not be representative of other areas of West Antarctica.

MT SURVEYING AT SOUTH POLE

Deep electrical resistivity investigations at the South Pole station were pursued for four principal reasons. First, such results would be the first ever sampling the interior of East Antarctica, revealing first-order structural information. Secondly, if MT can be done in the severe temperature conditions of the South Pole, it should be possible nearly anywhere on the continent. Thirdly, the resulting resistivity model determines the crustal response baseline for deep mantle resistivity profiles (100–1000 km depth range) that sorely need representation from this part of the globe (Egbert & Booker 1992; Everett & Schultz 1996). Fourthly, the South Pole station has been occupied continuously since 1956 and its facilities eased logistical requirements for this first MT deployment in the East Antarctic interior.

MT data collection procedure

MT sites were collected using the University of Utah system as simultaneous pairs spaced 6 km apart at the South Pole (Fig. 1), similar to CWA. Given the ~3 km of ice sheet thickness, this spatial sampling appears adequate because the ice serves to upward-continue the response from near-surface 'static' effects which trouble many land surveys (Groom & Bailey 1989; Pellerin & Hohmann 1990; Wannamaker 1999). Synchronized EM time-series from each five-channel site were transmitted via digital FM radio telemetry to the centrally located recording hut. Appendix A contains a description

of our MT system including the custom electrometer designed to handle the high electrode-firn contact impedance.

The profile was offset ~5 km from the South Pole station to avoid artificial EM interference from the station, although none was observed. The initial orientation of the profile was grid 210°, where grid north is Greenwich meridian, approximately normal to the Trans-Antarctic Mountains. The maximum distance of a sounding from the South Pole station was ~40 km, and location and navigation were by hand-held GPS. The average recording time per site was approximately 3 d. This is slow compared with most MT surveys on land, and was the result in part of the additional logistical requirements of Antarctica. It also was the result of serious wind-driven electrostatic noise which is discussed in Appendix B.

Observed MT data and its processing

Despite difficulties, patient surveying led to the acquisition of 10 good quality MT sites. When external noise sources were absent, high quality MT time-series such as those in Figs 2 and 3 were obtained. Under environmentally quiet (low wind) conditions, close correlations were seen between electric and magnetic fields taken simultaneously at two separated (6 km) sites at both high and low frequencies, with second-order differences at the lower frequencies related mainly to differences in geology between sites. Thunderstorms are essentially unheard of in Antarctica so that the spheric signals visible in Fig. 2 likely have propagated from the southern temperate or equatorial regions. The EM energy at $T < 0.01$ s wave periods is substantially damped through propagation over such distances, making it difficult to attain good shorter period responses, but this turns out to be unimportant for our geological interpretation of the data. Under the plane-wave assumption, variations in the vertical magnetic field (Fig. 3) would denote the presence of lateral resistivity heterogeneity in the earth (Vozoff 1991). However, at high latitudes, non-planar source components may also cause variations in H_z at the longer periods and need to be rejected during time-series processing (Mareschal 1986; Garcia *et al.* 1997; Pirjola 1998; Jones & Spratt 2002) as described below.

The apparent resistivity and impedance phase response for the sounding closest to the South Pole itself (SPLE03, Fig. 1) after robust processing are shown in Fig. 4. The most striking feature is the degree to which both modes of apparent resistivity fall from short period values around 5000 ohm m to long-period values of 10s or even <10 ohm m at other sites. High impedance phase values (>70°) accompany the fall in ρ_a. This response implies a substantial conductive section just below the ice sheet. Lateral variations in this section, or in deeper basement, may be causing the long-period response anisotropy. The response anisotropy is not strong here, and is usually weaker at the other sites. Low values of long-period apparent resistivity unfortunately signify weak MT **E**-field signals that are especially prone to contamination by environmental noise, such as from the wind.

Our processing for the middle and shorter periods ($T < 10s$) was based on a coherence-sorting scheme. Cascade decimation (Wight & Bostick 1980; Stodt 1983; Jones & Jodicke 1984) was used to obtain Fourier harmonics and spectral averages from short time-series subsets of data recorded simultaneously at two MT sites. Time-series segments at an individual site showing low multiple field coherence (<0.75) were rejected, and the remainder subject to remote reference processing using the corresponding data from the companion site (Gamble *et al.* 1979). This is similar to MT processing we have applied in temperate region surveys, and served well here.
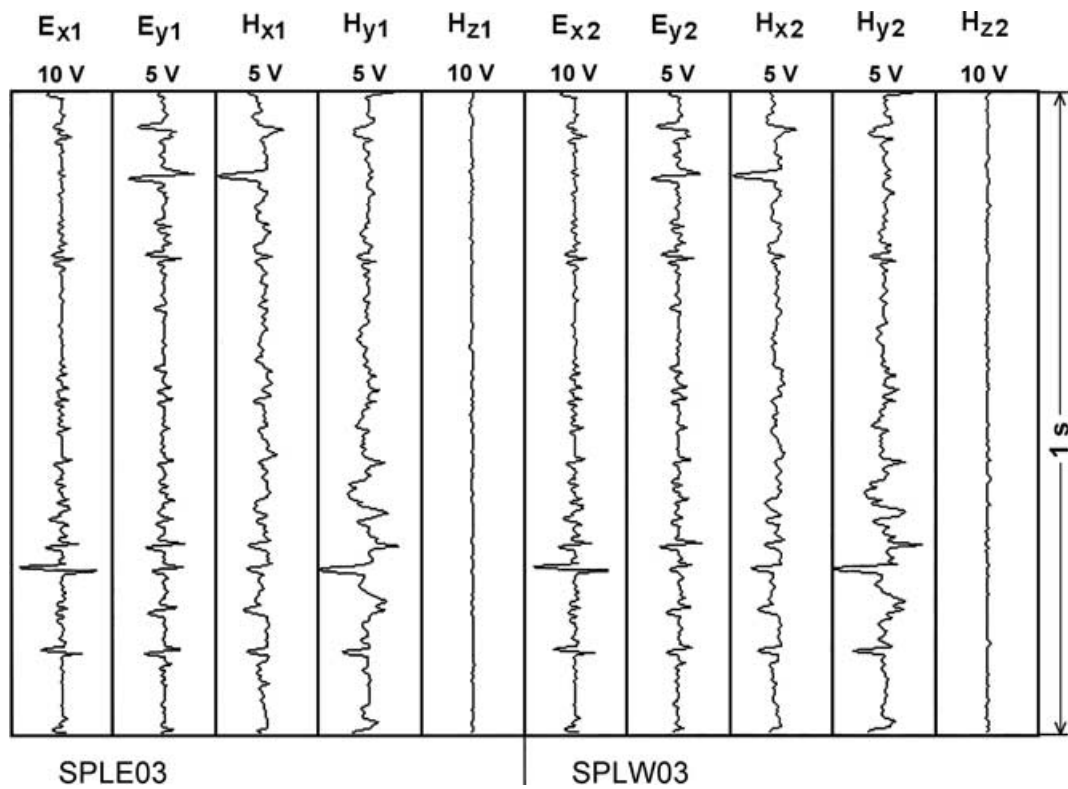
Figure 2. Sample time-series at sites SPLE03 (left-hand side) and SPLW03 (right-hand side) in the short period (atmospheric dominated) signal range. The time-series plot is ∼1.0 s in duration. Individual channel full-scale voltage ranges are printed by each channel number.
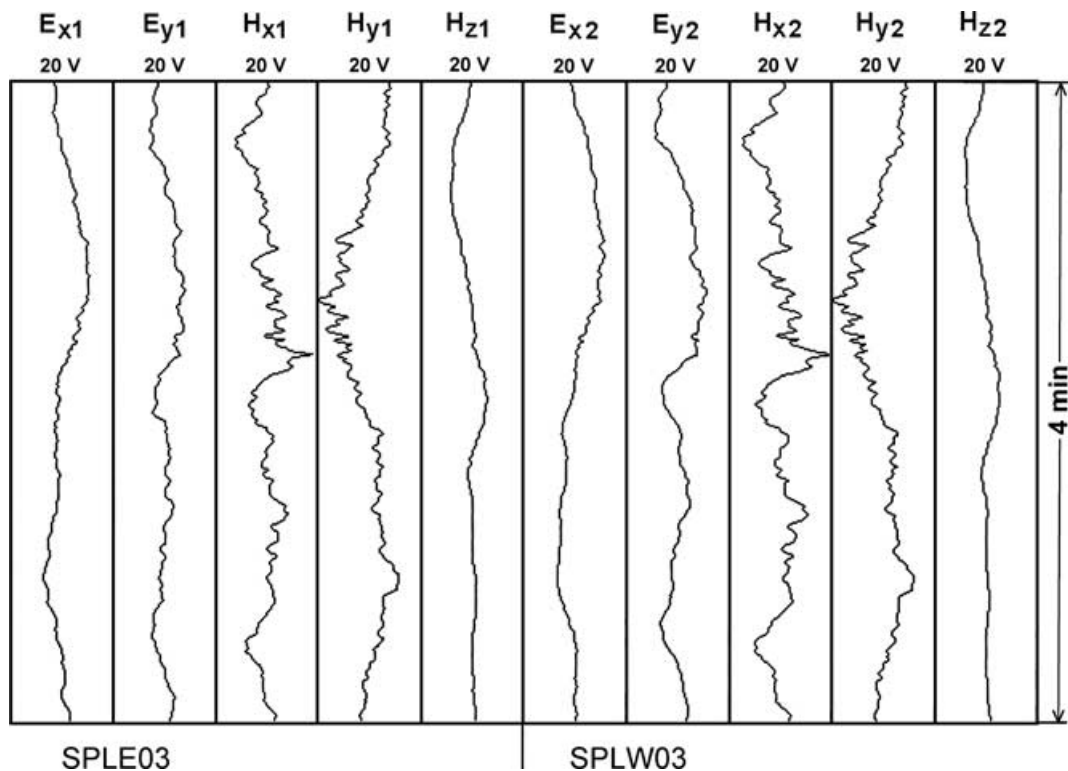

Figure 3. Sample time-series at sites SPLE03 (left-hand side) and SPLW03 (right-hand side) in the long-period (ionospheric dominated) signal range. Plotting conventions are as in Fig. 2. The time-series plot is ∼4.0 min in duration.
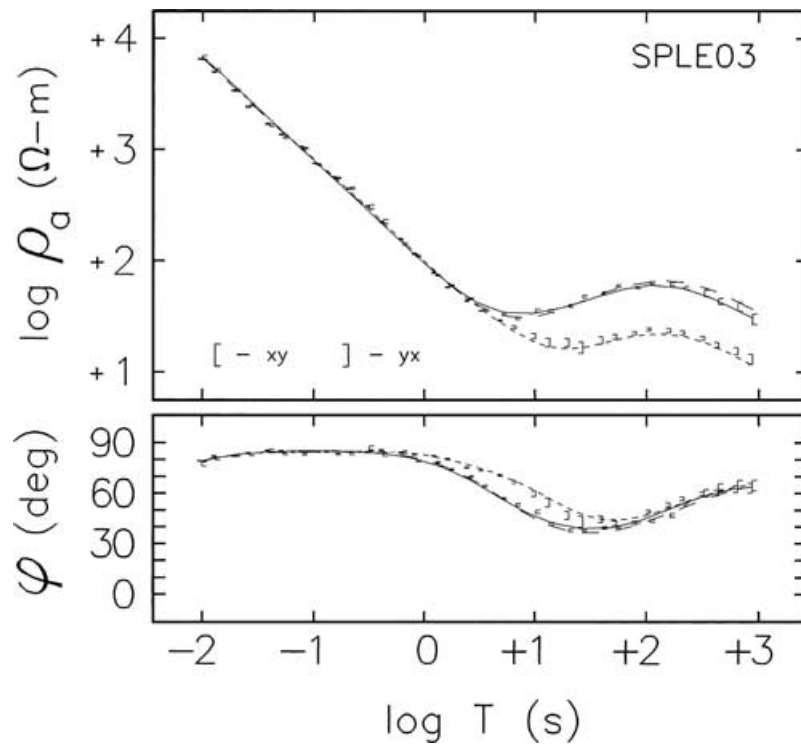
Figure 4. An example sounding from the transect located approximately 6 km from the South Pole station. The sounding location is denoted in Fig. 1 as E03. Nominal TE and TM mode quantities are ρ_{xy} and φ_{xy}, and ρ_{yx} and φ_{yx}, respectively, where the *x*-axis is oriented grid 288 for all sites and all periods are based on the apparent principal directions of K_z that are discussed in the text. Solid curves through ρ_{yx} and φ_{yx} are computed responses of TM mode inversion model of Fig. 9. Dashed curves are computed responses of joint TM-TE-K_{zy} inversion model of Fig. 9.

For longer periods, outliers due to non-plane-wave source effects can be important, and there is no guarantee that only good quality, plane wave estimates are retained by sorting according to high short-term multiple coherence. To remove outliers, a variant of robust processing based on jackknife methodology (Chave & Thompson 1989; Thompson & Chave 1991) was developed and applied. Here we emphasized removal of outliers in the vertical magnetic field similar to Jones & Spratt (2002). This proved effective, and in fact was necessary because only a small minority of the longer-period **E**-field data is of high coherence with **H** in this survey due to the prolonged wind noise. Such noise left too few high-quality **E**–**E** or **E**–**H** cross spectra for effective robust processing or coherence sorting based simply on the impedance. The sounding of Fig. 4 in fact is the only site where impedance-based coherence sorting and outlier removal was unambiguously possible and gave very good results. However, having this site fortunately allowed us to implement a robust scheme described below based upon using outlier removal of the vertical **H**-field tensor K_z as a proxy for outlier removal from the impedances at other sites where wind noise dominated the **E**-fields. The fidelity of the magnetic field records generally is very high for all sites; for the site in Fig. 4, approximately 95 per cent of the magnetic records are retained at a coherence cut-off of 0.96.

To process the data effectively, we utilized a three-step robust processing algorithm combining coherence sorting and jackknife methodology. First, minimal subsets of the pool of all available spectral cross-products at a given frequency were averaged and pre-sorted according to multiple coherence between the horizontal **H**-fields of the MT site pair to remove the few noisy **H**-field records. Next, all possible delete-one estimates (Thompson & Chave 1991) of a selected pair of complex transfer functions (Z_{xx}–Z_{xy}, Z_{yx}–Z_{yy} or

K_{zx}–K_{zy}) were computed from the surviving group of cross-products. Initially treating the real and imaginary parts of each transfer function separately, the mean and standard deviation of the ensemble of delete-one estimates, plus the individual estimate deviations from the mean, are calculated. The four resulting standard deviations of the real and imaginary parts of the selected pair of transfer functions are each compared with the maximum spread of the corresponding deviations from the mean of the individual delete-one estimates. The jackknife processing is terminated if the span of deviations from the means for each estimate is less than a specified value (nominally six times the standard deviation) for two successive iterations. Otherwise, for each complex transfer function of the selected pair, the delete-one estimate exhibiting the largest absolute deviation from the mean is identified and the set of cross-products which was excluded to calculate it is rejected, to complete the current iteration. If the termination test is not met as iterations progress then, pragmatically, this processing is terminated once a user-specified percentage (nominally 35 per cent) of the data not excluded by pre-sorting is rejected. Optionally, a final coherence sort of the surviving data can then be applied. For K_z specifically, this processing typically left several tens of sets of cross-products of good quality at the longest period ($\sim$1000 s), and correspondingly more at shorter periods, to calculate robust transfer functions.

For the site in Fig. 4 where high-quality **E**-fields could be recorded, two different jackknife processing runs were made subsequent to **H**-field pre-sorting; one to directly remove impedance outliers (JK) and the second to remove outliers in K_z (KZ). The effectiveness of outlier removal on reducing data scatter in K_z is exemplified in Fig. 5; the JK and KZ removal criteria yield essentially identical data points that are greatly improved from those of
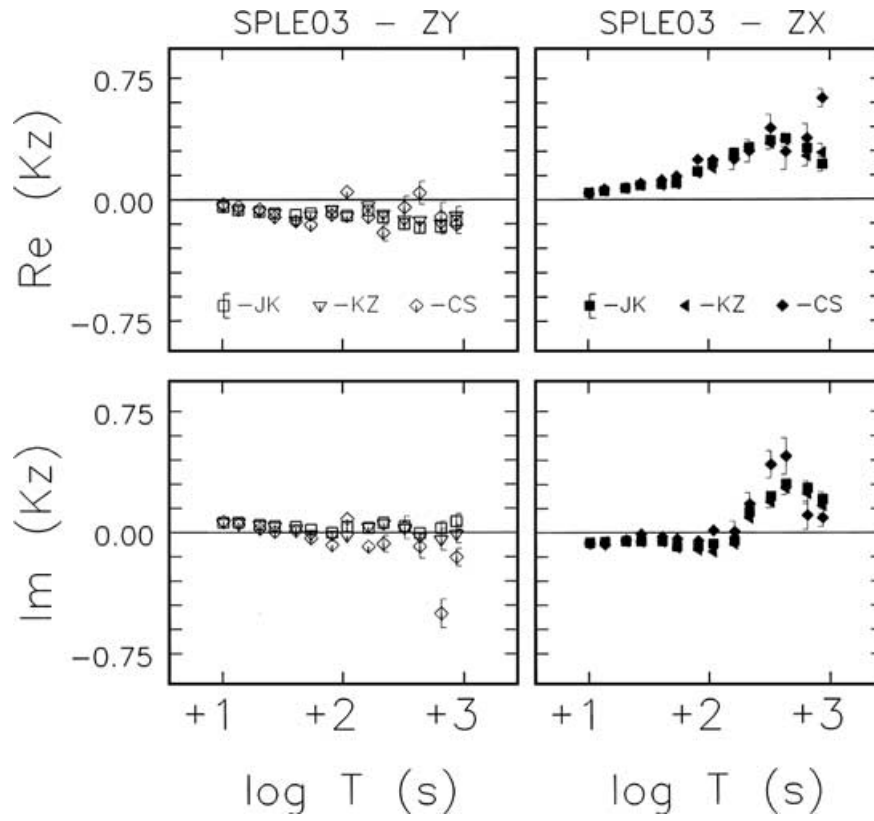
Figure 5. Vertical magnetic field transfer function estimates for MT site SPLE03 processed three ways: jackknife method on the impedance (JK), jackknife on the vertical **H**-field (KZ) and standard coherence sorting of the impedance (CS). Error bars are one standard deviation, plotted where larger than the data symbols.
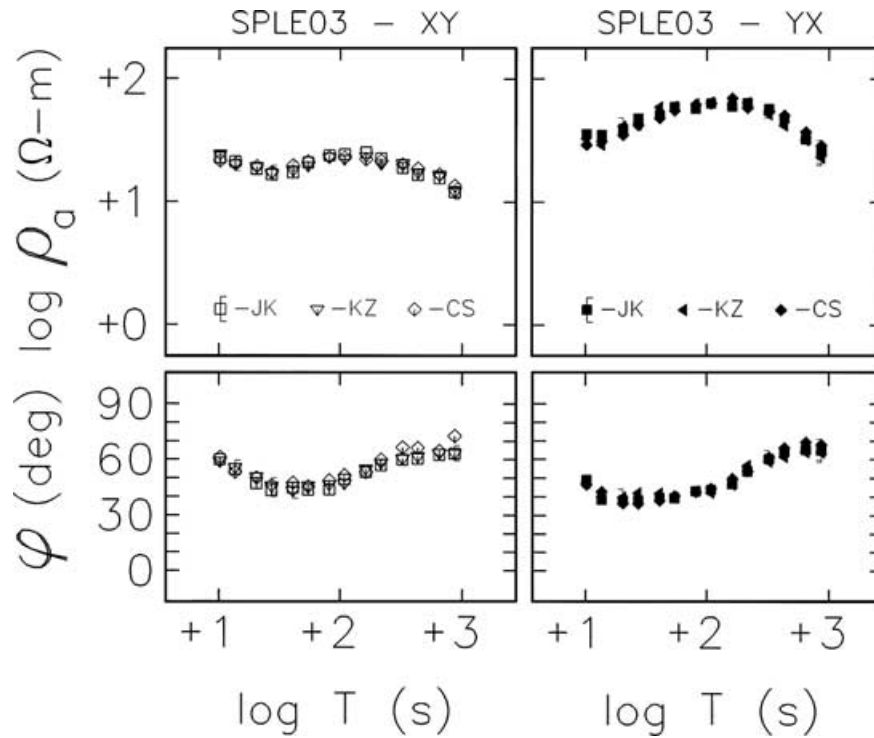

Figure 6. Apparent resistivity and impedance phase transfer function estimates for MT site SPLE03 processed three ways: jackknife method on the impedance (JK), jackknife on the vertical **H**-field (KZ) and standard coherence sorting of the impedance (CS). Error bars are one standard deviation, plotted where larger than the data symbols.

coherence sorting alone (CS). The difference between coherence-sorted and jackknife-processed impedance estimates is much less than for K_z, due to greater apparent stability of the CS results, with only a modest improvement in φ_{xy} visible in Fig. 6. The greater improvement in K_z response is consistent with other experience that source effects have stronger deleterious influence on the vertical magnetic field (Egbert 2002; Jones & Spratt 2002). Nevertheless, the similarity between the two jackknife processing results suggests that removal of outliers from one set of MT functions (e.g. vertical **H**-field) can serve as a proxy for outlier removal from other functions (e.g. impedance). Consequently, we performed jackknife processing of the K_z tensor elements at all sites, and computed bulk averages of the impedance values from the remaining spectra when wind noise appeared dominant. We presume these results are relatively free of non-planar source field effects.

Processing to remove outliers greatly smoothed the vertical magnetic field responses, and improved the impedance responses somewhat, but it did not substantially change the basic trends of the responses versus period from those by coherence sorting alone. This differs somewhat from the experience of Jones & Spratt (2002) perhaps because of the much lower apparent resistivities we encountered. Our values at long periods typically lie in the 10s of ohm m while those of Jones & Spratt (2002) were in the 1000s of ohm m. Because the non-plane-wave effects they encountered occurred mainly for $T > 100$ s, our lower resistivity environment should not experience similar effects until $T > 1000$ s according to basic EM

scaling (Grant & West 1965). Finally, although we emphasized K_z outlier removal, we did not specifically discriminate against high K_z values (*cf.* Jones & Spratt 2002) because we could not assume *a priori* that no significant lateral heterogeneity was present in the survey area.

Pseudosections of final impedance and vertical magnetic field quantities are compiled in Fig. 7. These are defined for an x-axis of grid 288, which is a counter-clockwise rotation of $12°$ from the original setup. This slight rotation is more compatible with principal axes of K_z, as noted below, and has only a very small effect on the appearance of the impedance results. The dramatic fall in ρ_a of both modes is clear over all sites, with long period variations presumably reflecting variations in subice lithology. The scatter visible in φ_{xy} for $T > 10$s is due to less favourable source field polarization and to E_x commonly being smaller than E_y. A mild increase in ρ_a for $T > 10$s is observed and accompanied by lower phase values in both modes, indicating the presence of higher resistivity below the subice conductor. At the longest periods, >100 s, both modes at all sites have higher phases and falling apparent resistivities again, suggestive of deeper conductive material which we will show lies in the lower crust and uppermost mantle.

The vertical magnetic field anomalies of K_{zy} are quite weak in our coordinate definition, implying that lateral gradients in resistivity along the profile are small. Because the corresponding TE impedance phase φ_{xy} shows long period values that are essentially isotropic relative to the TM mode, this further suggests little
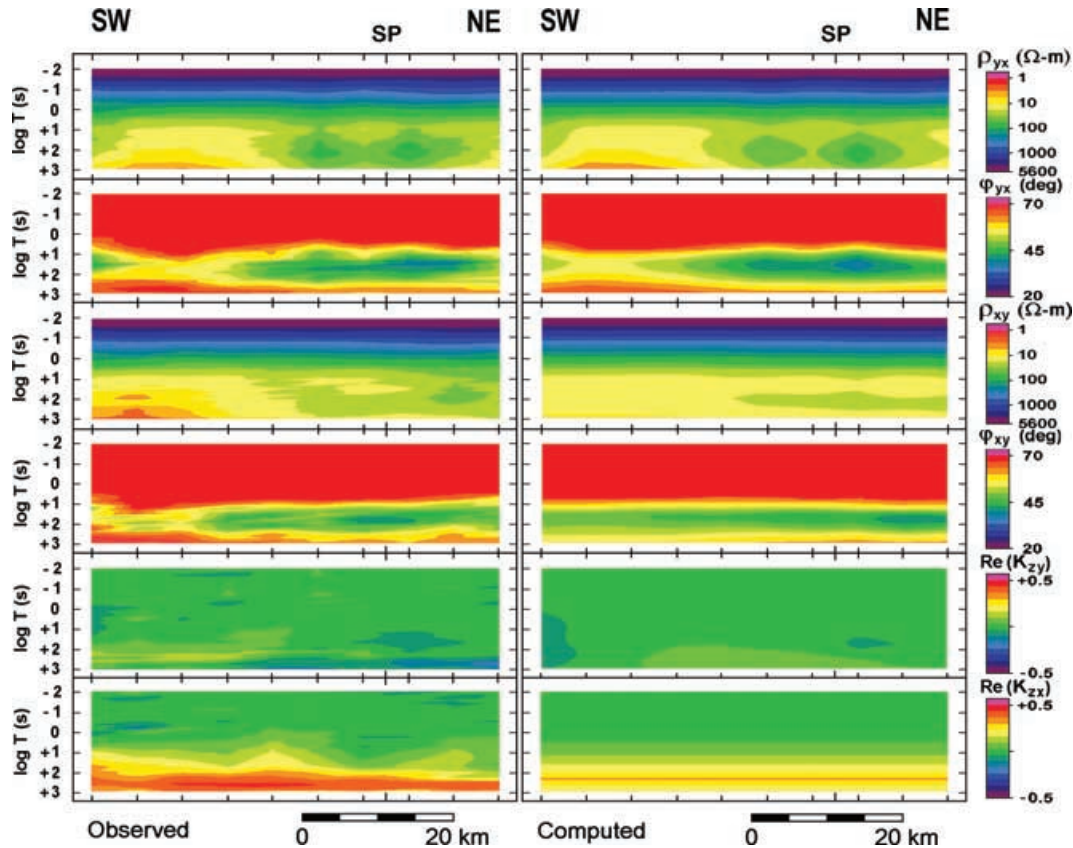

Figure 7. Pseudosections of observed (left-hand side) and modelled (right-hand side) apparent resistivity, impedance phase, and normalized vertical **H**-field quantities for the ten sites of the South Pole transect. In pseudosections, log period (T) defines the ordinate and horizontal distance defines the abscissa for contour plots of MT responses for all sites. Quantities ρ_{xy} and φ_{xy} are assigned to the TE mode for modelling while ρ_{yx} and φ_{yx} are assigned to the TM mode. Computations are for the joint TM-TE-K_{zy} inversion model of Fig. 9. The uniform contour plot of Re(K_{zx}) denotes response from inversion of integrated response curves to image SE–NW resistivity gradients seen in Fig. 10. Projection of the South Pole station is SP.

remaining influence of non-uniform field effects. In contrast, there is a significant anomaly in K_{zx} for $T \gtrsim 30$ s for all sites on the profile, which implies a large scale conductor lying roughly parallel to and grid southeast of our profile.

RESISTIVITY MODELS OF THE SOUTH POLE TRANSECT

Because the propagation of EM waves in the Earth at the periods of interest is diffusive, MT fields cannot resolve sharp structure in the subsurface without additional constraints (Parker 1994). One way to proceed is by solving for a limited number of resistivity parameters, such as in a discrete layered model, in a least-squares sense (e.g. Petrick *et al.* 1977). Alternately, the Earth model can be divided into several thousand incremental parameters or 'pixels', constrained as an ensemble to produce conservative model variations (de Groot-Hedlin & Constable 1990; Smith & Booker 1991), and often referred to as a minimum structure model. We consider both approaches.

Given the first-order similarity of all the sites, a quick initial interpretation is carried out by integrating the nominal TM (*yx*) mode impedance along the profile. Provided our measured responses are

not seriously undersampled laterally, this integration yields a single impedance sounding equivalent to that measured with one electrode line the length of the entire profile, so that the influence of lateral heterogeneity is effectively suppressed (Torres-Verdin & Bostick 1992; Wannamaker *et al.* 1997) (Fig. 8). The nominal error bars for the integrated impedance are smaller than those of any individual sounding because each original sounding contains independent information concerning the regional average profile. Although a physical basis for such an integration is established only for the TM mode, we apply it to the TE mode and vertical magnetic field quantities also and show that there is a single model of resistivity variation in the northwest-southeast direction normal to the profile which is consistent with all the quantities.

The integrated TM mode impedance is amenable to 1-D inversion which we carry out using an algorithm based on the Marquardt method described by Petrick *et al.* (1977). The best-fitting parameters of a five-layer earth are tabulated in Fig. 8 and the computed fit to the TM data is shown as solid curves (rms misfit of ~3.2). Starting layer thicknesses from the surface downward were 2.8 km (ice; Jiracek 1967; Bentley 1991), 2, 15 and 15 km. Initial resistivities were 10^5 ohm m for the ice and 10 ohm m for the other media. The
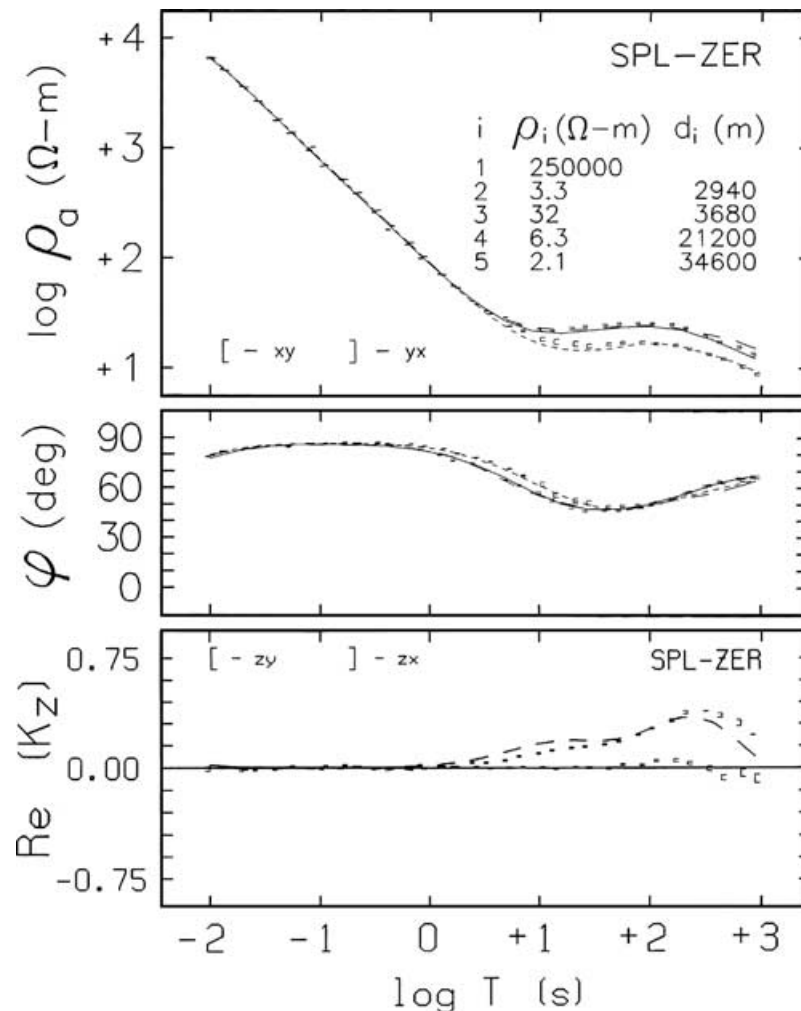

Figure 8. Integrated impedance and K_z sounding curves generated from the ten soundings of the transect. Inversion parameter values of five-layered earth fitting integrated TM mode impedance are tabulated in upper right-hand corner. Computed response of this 1-D model to the TM mode data is shown as solid curves. Dashed curves are fitted to TE (*xy*) and TM modes (*yx*) and Re(K_{zx}) of the inverse model of Fig. 10. Rollover in impedance phase to <90° at high frequencies was determined to be instrumental and due in part to contact impedance effects.

final ice thickness changed only slightly from the initial value and showed a parameter standard deviation of <3 per cent. We also performed 1-D inversions on both modes of each individual sounding; the resulting ice thicknesses remained within 150 m of 2.9 km with similarly small parameter standard deviations in all cases, indicating that little subice topography exists beneath our profile. However, the estimated ice resistivity is only somewhat larger than 10^4 ohm m (Fig. 8), which results from fitting the subtle rollover in φ_{yx} from near 90° at 0.1 s to ∼78° at 0.01 s. Ice resistivities >10^5 ohm m, which are more compatible with Antarctic radar and DC resistivity surveying (Bentley 1991; Shabtaie & Bentley 1995) keep phases near 90° up to 0.01 s. We believe the discrepancy is instrumental and due in part to the effects of electrode contact impedance at the shorter periods, as discussed in Appendix A. Ice values >10^5 ohm m are compatible with our MT data to periods as short as 0.1 s and cause negligible changes in the earth parameter values in 1-D inversion from those tabulated in Fig. 8.

The conductive layer below the ice in the 1-D model is ∼1 km thick and is of low resistivity (∼3 ohm m). Increasing the resistivity to 10 ohm m and allowing a greater thickness in the inversion produces a significantly poorer fit (e.g. ∼3° at $T = 10$s, not shown). The deeper crust is moderately more resistive, but only reaches a few tens of ohm m. However, because thin resistive layers are difficult to resolve with MT (Madden 1971; Vozoff 1991), higher resistivity domains of limited extent could exist with little influence on the data. Below ∼20 km depth, the lower crust and upper mantle resistivities become low (2–6 ohm m). These small values are surprising and suggest active tectonic processes below the polar plateau in this region, as discussed later.

2-D models of MT data are estimated through regularized inversion techniques intended to minimize model artefacts caused by data noise (Tarantola 1987). Our inversion algorithm uses the finite-element simulator of Wannamaker *et al.* (1987) and DeLugao & Wannamaker (1996) and damps model variations from an *a priori* structure (Tarantola 1987). As depth increases in the model, parameter thicknesses and widths expand to help equalize parameter influence on the MT response according to EM scaling (Grant & West 1965). The starting guess and *a priori* model for the 2-D inversions is a smooth 1-D profile derived from an analogous 1-D *a priori* inversion of the integrated TM mode impedance response of Fig. 8. The ice resistivity and thickness are set to 13 300 ohm m and 2960 m from the 1-D layered inversions. The 2-D inversions were ended when misfit reductions per iteration became <0.05 per cent. (*cf.* Wannamaker *et al.* 2002).

Two 2-D inversions models are presented in Fig. 9. The upper one is from inversion of the TM mode only, due to its likely lower sensitivity to finite strike (3-D) effects relative to the other MT quantities (Wannamaker 1999). The rms misfit of this model is ∼2.6 and the good fit of the TM response is exemplified in Fig. 3. The second model in Fig. 9 is from joint inversion of the TM and TE modes together with sK_{zy}. The computed response is not quite as close as for the TM mode only (Fig. 3), with an rms of ∼4.1, but still is good overall and the model resembles that of the TM-only calculation. The computations from the joint inversion are compared with the data in Fig. 7. In particular, the lateral variations in subice resistivity structure do not cause strong anomalies in the vertical **H**-field element K_{zy} (real part only plotted). The good agreement between all modes of MT data in the joint inversion
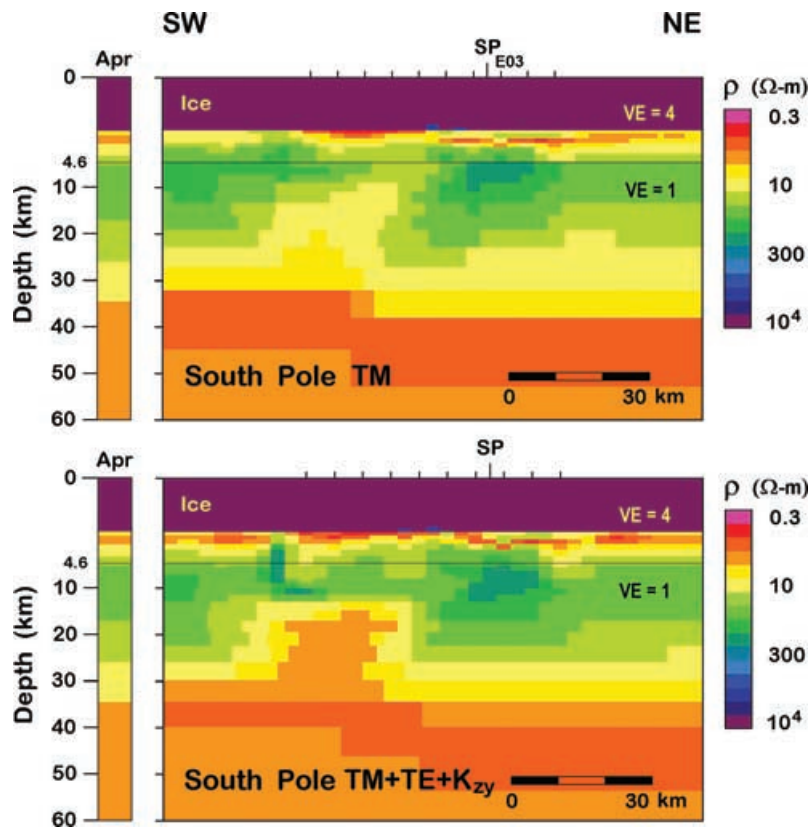

Figure 9. 2-D resistivity cross-sections from TM-only (top) and joint TM-TE-K_{zy} (bottom) inversions. The 1-D smooth resistivity profile (Apr) serving as *a priori* and starting models is shown as a column to the left-hand side of each section. Note the vertical exaggeration of 4:1 in the upper 4.6 km. Projection of the South Pole station is denoted by SP and of site SPLE03 by E03 along the top section.

suggests that the 2-D approximation is reasonable (Wannamaker 1999).

In both 2-D models, a pronounced conductive layer is visible beneath the ice sheet within which there are thickness variations reproducing the fundamental lateral variations especially in the TM response. Mid-crustal resistivities are somewhat variable but reach 100 ohm m in places. Low resistivity in the deep crust and upper mantle is also seen, as implied previously from the falling ρ_a and 1-D models. Sensitivity tests using the integrated impedance data suggest that such low resistivities persist to depths of at least 60 km. Under the western portion of the transect, a lower resistivity zone is seen extending upward from the lower crust to depths of ∼10 km. This is seen in both the TM only and joint inversion models, although its somewhat more pronounced nature in the joint model may be due in part to finite strike effects in the overlying shallow conductive subice section as reflected in particularly low values of ρ_{xy} and high φ_{xy} at the southwest end.

We attempt to interpret the strong response in K_{zx} at all sites in our profile by making use of the integrated response curves of Fig. 8. The model framework is rotated counter-clockwise by 90° so that the integrated Z_{yx} is treated as TE, Z_{xy} is treated as TM and K_{zx} is treated as TE mode K_{zy} for the sake of 2-D inversion. Use of the integrated responses assumes that the effects of upper crustal heterogeneity have essentially been integrated out. Although this obviously is a small summary data set providing limited structural information, we are able to derive a 2-D image in the SE–NW direction that is compatible with the three integrated curves.

The resulting 2-D image from the integrated response curves is presented in Fig. 10. The computed response in Re(K_{zx}) shown in Fig. 8 has an rms misfit of ∼5.4. The K_{zx} data are diagnostic in implying a large-scale decrease in resistivity ∼30 km to the southeast of the South Pole. This structure runs approximately parallel to our profile of stations and perpendicular to the TAM. Decreases in resistivity to the southeast in this model are distributed over all depths starting from just below the ice, because the regularized inversion method provides a smooth model and the integrated sounding data provide little depth discrimination. An additional southeast-northwest profile of stations approximately the same length as that we acquired would improve resolution of this feature substantially.

GEOLOGICAL IMPLICATIONS OF SOUTH POLE RESISTIVITY STRUCTURE

The conductive layer of variable thickness directly under the ice sheet is strongly suggestive of sedimentary rocks of substantial porosity or of clay or organic matter content (e.g. Wannamaker & Doerner 2002). Tentatively, it is correlated with the previously described Beacon Supergroup, although there may be younger sedimentary components associated with the projection of the Wilkes subglacial basin (Lythe *et al.* 2001). This basin in turn may be a flexural downwarp associated with uplift of the TAM (ten Brink *et al.* 1997). The MT results confirm the conjecture of Bentley (1991) that the absence of returned energy in their seismic refraction survey was the result of a thick, low-velocity layer (sediments). Return energy also may have been prohibited by scattering from the variable sedimentary thickness suggested by the lateral changes in conductance of the subice conductor.

The resistivity of the lowermost crust and upper mantle beneath the South Pole region is strikingly low. At face value, it would suggest an active tectonic explanation with attendant high temperature fluids or melting for uplift of the polar plateau in this region (*cf.* Wannamaker *et al.* 1997). This may seem at odds with the status of East Antarctica as a cratonic terrane, but there are some indications of activity. For example, in a compilation of subice areas of high radar reflectivity interpreted to indicate fresh water lakes, including several near the South Pole, Siegert (2000) proposed that heat flow through much of the East Antarctic lithosphere could be ∼50 m Wm^{-2} or more. Some studies suggesting seismic group velocities slower than those typical of shield regions (e.g. Gamburtsev Mountains) may be explained by large-scale lateral heterogeneity and cryptic tectonic activity (Bentley 1991; Bell & Karl 1999). Depending upon the timing of the onset of activity, thermal effects may not yet have propagated to shallow levels of the crust (*cf.* Bodell & Chapman 1982). Our results are not consistent with an effective elastic thickness of 80 km as modelled for southern Victoria Land (ten Brink *et al.* 1997), although that is considerably removed from our area of study. Cratonic S-velocities are characteristic of interior East Antarctica, but the South Pole is on a steep lateral gradient in
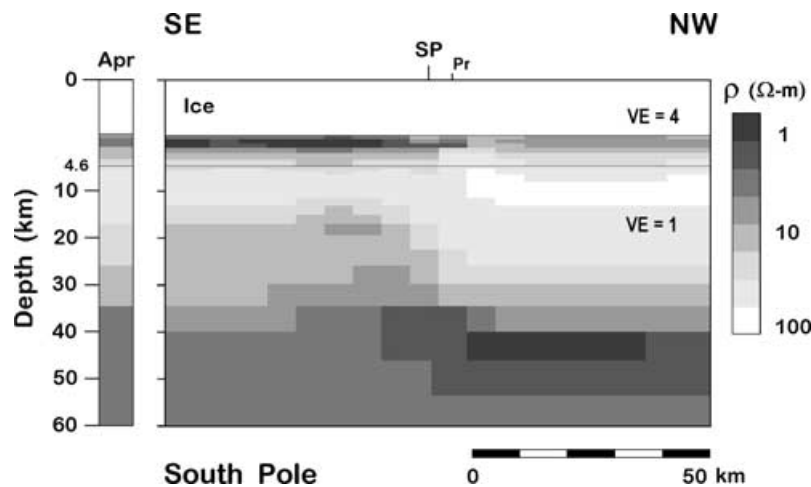

Figure 10. 2-D resistivity cross-section from joint TM-TE-K_{zy} inversion of the integrated sounding data of Fig. 8. The 1-D smooth resistivity profile (Apr) serving as *a priori* and starting models is shown as a column to the left-hand side of the section and is the same as those of Fig. 9. Projection of the South Pole station is denoted by SP and of the site profile by Pr. The integrated sounding is considered to reside at Pr for the inversion.

all velocity models so far, clouding a comparison with our resistivity structure.

An alternative non-thermal explanation for low resistivity in the lower crust and upper mantle, namely graphite, is given lower priority than that of fluids or melts. Although there are exceptions in areas of former deep sedimentary underthrusting (Wannamaker 2000), most lower crustal and upper mantle terranes have oxidation states near the quartz–fayalite–magnetite (QFM) buffer (Winkler 1979; Gaetani & Grove 1999; Canil 2002). In thermal regimes where temperatures exceed ∼500°C, graphite under QFM is unstable (Frost & Bucher 1994; Pasteris 1999). Moreover, the deep conductivity structure we resolve appears to be quite isotropic. Deep terranes with high conductivity interpreted to be controlled by graphite tend to have high apparent anisotropy due to stress orientation or rock fabric during deposition or emplacement (Hjelt & Korja 1993; Mareschal 1995; Wannamaker 2000), although there may be exceptions (Jones *et al.* 2001). Graphite could be important in the narrower, mid-crustal conductive structures imaged near the western end of our profile or to the southeast of the South Pole because temperatures are likely cooler at these levels making metamorphic fluids less likely and graphite more stable (Wannamaker 2000).

The degree of extensional activity in Antarctica today is limited, perhaps related to its being surrounded by oceanic ridges, so that the volcanism and thermal processes are hypothesized to stem from mantle plume processes (Hole & LeMasurier 1994; LeMasurier & Landis 1996). Continents are estimated to migrate over ∼5 hotspot plumes every 150 Myr on average that may contribute up to one-third of lower crustal material (Condie 1999; Johnston & Thorkelson 2000). Plume fronts are modelled to interact with lithospheric basal 'topography', thereby localizing zones of melting and thermal processes (Burke 1996; Sleep 1997; Ebinger & Sleep 1998; Maza *et al.* 1998; Ayadi *et al.* 2000), which may explain regionalized East Antarctic uplifts such as the Gamburtsev–Vostok areas. Additionally, Lake Vostok with its great depth is reminiscent of rift basins and, if so, active geothermal vents may constitute a favourable energy regime for life forms in this extreme environment (Bell & Karl 1999). Timing of initiation of any activity under East Antarctica is difficult to bracket, but Fitzgerald & Stump (1997) resolve at least three distinct episodes of uplift affecting the TAM closer to the South Pole. In addition to possible plume-related causes, the thermal state under the South Pole may be enhanced by thermal encroachment including perhaps non-uniform extensional components from relatively active West Antarctica, such as the somewhat analogous situation at the Great Basin–Colorado Plateau transition in the western United States (Bodell & Chapman 1982; Storey & Alabaster 1991; Rocholl *et al.* 1995; Wannamaker *et al.* 2001).

CONCLUSIONS

High-quality MT measurements may be gained from the Antarctic interior with proper attention to instrument design and time-series processing. Incorporation of high-impedance electrode buffer amplifiers and non-reactive electrodes can yield electric field records of high fidelity over thick ice. The robust removal of non-plane-wave outliers with emphasis on the vertical magnetic field appears to yield stable MT transfer functions for both the impedance and the vertical magnetic field. The principal impediment to high quality MT data that we experienced was wind-induced electrostatic noise in the polar ice due to blowing ice particles, particularly over survey areas with conductive crustal sections that reduce MT **E**-field signal. Signal-to-noise ratio may be improved by lengthening the **E**-field bipoles and by ensuring that a locally level surface is defined

around the implanted electrodes. Magnetic field recording appeared to present no special problems relative to surveying in temperate climates, although calibration factors appropriate to low operating temperatures should be ensured.

Our MT results have provided some of the first definitive indications of subice structure and physical state below the South Pole region. A substantial and widespread sedimentary section with significant porosity or matured organic content is inferred just below the ice sheet, corroborating earlier conjecture from refraction seismic data. The section may correlate with the regionally extensive Paleozoic Beacon Supergroup with possible younger components. Deep resistivity structure of the South Pole region at present appears to differ from that typical of cratonic lithosphere worldwide in exhibiting low resistivity in the lower crust and upper mantle. We believe thermal activity generating high-temperature fluids or melts is more likely than solid phases for explaining the low resistivity, although the interpretation is not unique. Regionalized plume-related dynamics in the deep lithosphere may be the dominant process behind thermal activity, with possible contributing influence from nearby West Antarctica.

REFERENCES

Ayadi, A., Dorbath, C., Lesquer, A. & Bezzeghoud, M., 2000. Crustal and upper mantle velocity structure of the Hoggar swell (Central Sahara, Algeria), *Phys. Earth planet. Inter.,* **118,** 111–123.

Barrett, P.J., 1991. The Devonian to Jurassic Beacon Supergroup of the Transantarctic Mountains and correlatives in other parts of Antarctica, in *The Geology of Antarctica,* ed. Tingey, R.J., pp. 120–152, Clarendon, Oxford.

Beblo, M. & Liebig, V., 1990. Magnetotelluric measurements in Antarctica, *Phys. Earth planet. Inter.,* **60,** 89–99.

Behrendt, J.D., 1999. Crustal and lithospheric structure of the West Antarctic Rift system from geophysical investigations—a review, *Global Planet. Change,* **23,** 25–44.

Behrendt, J.D., LeMasurier, W.E., Cooper, A.K., Tessensohn, F., Trehu, A. and D. Damaske, 1991. Geophysical studies of the West Antarctic rift system, *Tectonics,* **10,** 1257–1273.

Behrendt, J.D., Blankenship, D.D., Finn, C.A., Bell, R.E., Sweeney, R.E., Hodge, S.M. & Brozena, J.M., 1994. CASERTZ aeromagnetic data reveal late Cenozoic flood basalts (?) in the West Antarctic rift system, *Geology* **22,** 527–530.

Bell, R.E. & Karl, D.M., 1999. Evolutionary processes a focus of decade-long ecosystem study of Antarctic's Lake Vostok, *EOS, Trans. Am. geophys. Un.,* **80**(48), 573, 579.

Bentley, C.R., 1973. Crustal structure of Antarctica, *Tectonophysics* **20,** 229–240.

Bentley, C.R., 1991. Configuration and structure of the subglacial crust, in *The Geology of Antarctica,* pp. 335–364, ed. Tingey, R.J., Clarendon, Oxford.

Bentley, C.R. & Clough, J.W., 1970. Antarctic subglacial structure from seismic refraction measurements, in *Antarctic geology and geophysics,* pp. 292–297, ed. Adie, R.J., Universitetsforlaget, Oslo.

Blankenship, D.D., Bell, R.E., Hodge, S.M., Brozena, J.M., Behrendt, J.C. & Finn, C.A., 1993. Active volcanism beneath the West Antarctic ice sheet and implications for ice-sheet stability, *Nature,* **361,** 526–529.

Blankenship, D.D. *et al.,* 2001. Geologic controls on the initiation of rapid basal motion for West Antarctic ice streams: a geophysical perspective including new airborne radar sounding and laser altimetry results, in *The West Antarctic Ice Sheet: Behavior and Environment,* pp. 105–121, eds Alley, R.B. & Bindschadler, R.A., Antarctic Res. Ser., 77, Amer. Geophys. Union, Washington, DC.

Bodell, J.M. & Chapman, D.S., 1982. Heat flow in the north-central Colorado Plateau, *J. geophys. Res.,* **87,** 2869–2884.

Borg, S.G. & DePaolo, D.J., 1994. Laurentia, Australia, and Antarctica as a Late Proterozoic supercontinent: constraints from isotopic mapping, *Geology* **22,** 307–310.

Burke, K., 1996. The African plate, *S. Afr. J. Geol.,* **99,** 341–409.

Cande, S.C., Stock, J.M., Muller, R.D. & Ishihara, T., 2000. Cenozoic motion between East and West Antarctica, *Nature,* **404,** 145–150.

Canil, D., 2002. Vanadium in peridotites: mantle redox and tectonic environments: Archean to present, *Earth planet. Sci. Lett.,* **95,** 75–90.

Chave, A.D. & Thompson, D.J., 1989. Some comments on magnetotelluric response function estimation, *J. geophys. Res.,* **94,** 14 215–14 225.

Clarke, T.S., Burkholder, P.D., Smithson, S.B. & Bentley, C.R., 1997. Optimum seismic shooting and recording parameters and a preliminary crustal model for the Byrd Subglacial Basin, Antarctica, in *The Antarctic Region: Geological Evolution and Processes,* pp. 485–493, ed. Ricci, C.A., Terra Antarc. Publ., Sienna.

Condie, K.C., 1999. Mafic crustal xenoliths and the origin of the lower continental crust, *Lithos,* **46,** 95–101.

Dalziel, I.W.D., 1991. Pacific margins of Laurentia and East Antarctica–Australia as a conjugate rift pair: evidence and implications for an Eocambrian supercontinent, *Geology* **19,** 598–601.

Dalziel, I.W.D., 1997. Neoproterozoic–Paleozoic geography and tectonics: review, hypothesis, environmental speculation, *Geol. Soc. Am. Bull.,* **108,** 16–42.

Dalziel, I.W.D. & Lawver, L.A., 2001. The lithospheric setting of the West Antarctic ice sheet, in *The West Antarctic ice sheet: behavior and environment,* pp. 105–121, eds Alley, R.B. & Bindschadler, R.A., Antarctic Res. Ser., 77, Amer. Geophys. Union, Washington, DC.

Danesi, S. & Morelli, A., 2000. Group velocity of Rayleigh waves in the Antarctic region, *Phys. Earth planet. Inter.,* **122,** 55–66.

Davey, F.J. & Brancolini, G., 1995. The Late Mesozoic and Cenozoic structural setting of the Ross Sea region, in *Geology and Seismic Stratigraphy of the Antarctic Margin,* pp. 167–182, eds Cooper, A.K., Barker, P.F. & Brancolini, G., Antarctic Res. Ser., 68, AGU.

de Groot-Hedlin, C.D. & Constable, S.C., 1990. Occam's inversion to generate smooth, two-dimensional models from magnetotelluric data, *Geophysics,* **93,** 1613–1624.

DeLugao, P.P. & Wannamaker, P.E., 1996. Calculating the two-dimensional magnetotelluric Jacobian in finite elements using reciprocity, *Geophys. J. Int.,* **127,** 806–810.

Ebinger, C.J. & Sleep, N.H., 1998. Cenozoic magmatism throughout east Africa resulting from impact of a single plume, *Nature,* **395,** 788–791.

Edminister, J.A., 1965. *Schaum's outline of theory and problems of electric circuits,* p. 289, McGraw-Hill, New York.

Egbert, G.D., 2002. Processing and interpretation of electromagnetic induction array data, *Surv. Geophys.,* **23,** 207–249.

Egbert, G.D. & Booker, J.R., 1992. Very long period magnetotellurics at Tucson observatory: implications for mantle conductivity, *J. geophys. Res.,* **97,** 15 099–15 112.

Everett, M.E. & Schultz, A., 1996. Geomagnetic induction in a heterogeneous sphere: azimuthally symmetric test computations and the response of an undulating 660-km discontinuity, *J. geophys. Res.,* **101,** 2765–2783.

Fitzgerald, P., 1994. Thermochronologic constraints on post-Paleozoic tectonic evolution of the central Trans Antarctic Mountains, Antarctica, *Tectonics,* **13,** 818–836.

Fitzgerald, P.G. & Stump, E., 1997. Cretaceous and Cenozoic episodic denudation of the Transantarctic Mountains, Antarctica: new constraints from apatite fission track thermochronology in the Scott Glacier region, *J. geophys. Res.,* **102,** 7747–7765.

Fournier, H.G., 1994. Geophysical studies of the Antarctic peninsula, *Acta. Geod. Geoph. Hung.,* **29,** 19–38.

Frost, B.R. & Bucher, K., 1994. Is water responsible for geophysical anomalies in the deep continental crust? A petrological perspective, *Tectonophysics* **231,** 293–309.

Gaetani, G.A. & Grove, T.L., 1999. Wetting of mantle olivine by sulfide melt: implications for Re/Os ratios in mantle peridotite and late stage core formation, *Earth planet. Sci. Lett.,* **169,** 147–163.

Gamble, T., Goubau, W. & Clarke, J., 1979. Magnetotellurics with a remote reference, *Geophysics,* **44,** 53–68.

Garcia, X., Chave, A.D. & Jones, A.G., 1997. Robust processing of magnetotelluric data from the auroral zone, *J. Geomag. Geoelectr.,* **49,** 1451–1468.

Grant, F.S. & West, G.F., 1965. *Interpretation Theory in Applied Geophysics,* p. 584, McGraw-Hill, New York.

Groom, R.W. & Bailey, R.C., 1989. Decomposition of magnetotelluric impedance tensor in the presence of local three-dimensional galvanic distortion, *J. geophys. Res.,* **94,** 1913–1925.

Hessler, V.P. & Jacobs, J., 1966. A telluric current experiment on the Antarctic ice cap, *Nature,* **210,** 190–191.

Hjelt, S.-E. & Korja, T., 1993. Lithospheric and upper mantle structures, results of electromagnetic soundings in Europe, *Phys. Earth planet. Inter.,* **79,** 137–177.

Hole, M.J. & LeMasurier, W.E., 1994. Tectonic controls on the geochemical composition of Cenozoic, mafic alkaline volcanic rocks from West Antarctica, *Contr. Min. Petr.,* **117,** 187–202.

Humphreys, E.D. & Dueker, K.G., 1994. Physical state of the western US mantle, *J. geophys. Res.,* **99,** 9635–9650.

Jiracek, G.R., 1967. Radio sounding of Antarctic ice, Research Ser. Rep. 67–1, Geophys. & Polar Res. Ctr., p. 127, Dept Geol., Univ. Wisc., Madison.

Johnston, S.T. & Thorkelson, D.J., 2000. Continental flood basalts: episodic magmatism above long-lived hotspots, *Earth planet. Sci. Lett.,* **175,** 247–256.

Jones, A.G., 1992. Electrical conductivity of the continental lower crust, in *Continental lower crust,* pp. 81–143, eds Fountain, D.M., Arculus, R.J. & Kay, R.W., Elsevier, Amsterdam.

Jones, A.G., 1999. Imaging the continental upper mantle using electromagnetic methods, *Lithos,* **48,** 570–580.

Jones, A.G. & Jodicke, H., 1984. Magnetotelluric transfer function estimation improvement by a coherence-based rejection technique, 54th Soc. Explor. Geophys. Ann. Mtg, Atlanta, Dec. 2–6, Ext. Abstr., Tulsa, OK, 51–55.

Jones, A.G. & Spratt, J., 2002. A simple method for deriving the uniform field MT responses in the auroral zone, *Earth Planets Space,* **54,** 443–450.

Jones, A.G., Ferguson, I.J., Chave, A.D., Evans, R.L., Spratt, J. & Garcia, X., 2001. The electrical structure of the Slave craton, *Geology* **29,** 423–426.

Karlstrom, K.E., Ahall, K.-I., Harlan, S.S., Williams, M.L., McLelland, J. & Geissman, J.W., 2001. Long-lived (1.8–1.0 Ga) convergent orogen in southern Laurentia, its extensions to Australia and Baltica, and implications for refining Rodinia, *Precamb. Res.,* **111,** 5–30.

Kong, X., Zhang, J. & Jiao, C., 1993. Deep electrical conductivity structure in the region of Great Wall station, Fildes peninsula, west Antarctica, *Antarctic Res., Chinese Edn,* **5,** 40–47.

Kong, X., Zhang, J. & Jiao, C., 1994. Magnetotelluric deep sounding study in the region of Zhongshan station, East Antarctica, *Antarctic Res., Chinese Edn,* **6,** 32–36.

LeMasurier, W.E. & Landis, C.A., 1996. Mantle-plume activity recorded by low-relief erosion surfaces in West Antarctica and New Zealand, *Geol. Soc. Am. Bull.,* **108,** 1450–1466.

LeMasurier, W.E. & Rex, D.C., 1991. The Marie Byrd Land volcanic province and its relation to the Cainozoic West Antarctic rift system, in *The Geology of Antarctica,* pp. 249–284, ed. Tingey, R.J., Clarendon, Oxford.

Lowry, A.R., Ribe, N.M. & Smith, R.B., 2000. Dynamic elevation of the Cordillera, western United States, *J. geophys. Res.,* **105,** 23 371–23 390.

Lythe, M.B., Vaughan, D.G. & the BEDMAP consortium, 2001. BEDMAP: a new ice thickness and subglacial topographic model of Antarctica, *J. geophys. Res.,* **106,** 11 335–11 351.

MacGorman, D.R. & Rust, W.D., 1998. *The Electrical Nature of Storms,* p. 422, Oxford University Press, New York.

Madden. T.R., 1971. The resolving power of geoelectric measurements for delineating resistive zones within the crust, in *The Structure and Physical Properties of the Earth's Crust,* AGU Mono. 14, pp. 95–105, AGU, Washington, DC.

Mareschal, M., 1986. Modelling of natural sources of magnetospheric origin in the interpretation of regional induction studies: a review, *Surv. Geophys.,* **8,** 261–300.

Mareschal, M., 1995. Archaean cratonic roots, mantle shear zones and deep electrical anisotropy, *Nature,* **375,** 134–137.

Maza, M., Briqueu, L., Dautria, J.-M. & Bosch, D., 1998. The Achkal Oligocene ring complex: Sr, Nd, Pb evidence for transition between tholeiitic and alkali Cenozoic magmatism in Central Hoggar (South Algeria), Sci. Terre Planet., *C.R. Acad. Sci., Paris,* **327,** 167–172.

Parker, R.L., 1994. *Geophysical Inverse Theory,* p. 386, Princeton University Press, Princeton.

Pasteris, J.D., 1999. Causes of the uniformly high crystallinity of graphite in large epigenetic deposits, *J. Struct. Geol.,* **17,** 779–787.

Pellerin, L. & Hohmann, G.W., 1990. Transient electromagnetic inversion: a remedy for magnetotelluric static shifts, *Geophysics,* **55,** 1242–1250.

Petrick, W.R., Pelton, W.H. & Ward, S.H., 1977. Ridge-regression inversion applied to crustal resistivity sounding data from South Africa, *Geophysics*, **42,** 995–1005.

Pirjola, R.J., 1998. Modeling the electric and magnetic fields at the Earth's surface due to an auroral electrojet, *J. Atmos. Solar Terres. Phys.,* **60,** 1139–1148.

Reynolds, J.M., 1985. Dielectric behaviour of firn and ice from the Antarctic peninsula, *J. Glaciol.,* **31,** 253–262.

Ritzwoller, M.H., Shapiro, N.M., Levshin, A.L. & Leahy, G.M., 2001. Crustal and upper mantle structure beneath Antarctica and surrounding oceans, *J. geophys. Res.,* **106,** 30 645–30 670.

Rocholl, A., Stein, M., Molzahn, M., Hart, S.R. & Worner, G., 1995. Geochemical evolution of rift magmas by progrssive tapping of a stratified mantle source beneath the Ross Sea Rift, Northern Victoria Land, Antarctica, *Earth planet. Sci. Lett.,* **131,** 207–224.

Rodgers, J.J.W., Unrug, R. & Sultan, M., 1995. Tectonic assembly of Gondwana, *J. Geodyn.,* **19,** 1–34.

Roult, G., Rouland, D. & Montagner, J.P., 1994. Antarctica II: upper-mantle structure from velocities and anisotropy, *Phys. Earth planet. Inter.,* **84,** 33–57.

Schmidt, S. & Dent, J.D., 1993. A theoretical prediction of the effects of electrostatic forces on saltating snow particles, *J. Glaciol.,* **18,** 234–238.

Sen, V., Stoffa, P.L., Dalziel, I.W.D., Blankenship, D.D., Smith, A.M. & Anandakrishnan, S., 1998. Seismic surveys in central West Antarctica: data and processing examples from the ANTALITH field tests (1994–1995), *Terra Antarctica,* **5,** 761–772.

Shabtaie, S. & Bentley, C.T., 1995. Electrical resistivity sounding of the East Antarctic ice sheet, *J. geophys. Res.,* **100,** 1933–1954.

Siegert, M.J., 2000. Antarctic subglacial lakes, *Earth-Sci. Rev.,* **50,** 29–50.

Sleep, N.H., 1997. Lateral flow and ponding of starting plume material, *J. geophys. Res.,* **102,** 10 001–10 012.

Smith, J.T. & Booker, J.R., 1991. Rapid inversion of two and three dimensional magnetotelluric data, *J. geophys. Res.,* **96,** 3905–3922.

Sonder, L.J. & Jones, C.H., 1999. Western United States: how the west was widened, *Annu. Rev. Earth planet. Sci.,* **27,** 417–462.

Storey, B.C. & Alabaster, T., 1991. Tectonomagmatic controls on Gondwana break-up models: evidence from the proto-Pacific margin of Antarctica, *Tectonics,* **10,** 1274–1288.

Stodt, J.A., 1983. Processing of conventional and remote reference magnetotelluric data, *PhD thesis,* p. 223, University of Utah.

Stratton, J.A., 1941. *Electromagnetic Theory,* p. 615, McGraw-Hill, New York.

Tarantola, A., 1987. *Inverse Problem Theory,* p. 613, Elsevier, New York.

ten Brink, U.S., Bannister, S., Beaudoin, B.C. & Stern, T.A., 1993. Geophysical investigations of the tectonic boundary between East and West Antarctica, *Science,* **261,** 45–50.

ten Brink, U.S., Hackney, R.I., Bannister, S., Stern, T.A. & Makovsky, Y., 1997. Uplift of the Trans Antarctic Mountains and the bedrock beneath the East Antarctic ice sheet, *J. geophys. Res.,* **102,** 27 603–27 621.

Thompson, D.J. & Chave, A.D., 1991. Jackknifed error estimates for spectra, coherences, and transfer functions, in *Advances in Spectrum Analysis and Array Processing,* pp. 58–113, ed. Haykin, S., Prentice Hall, Englewood Cliffs.

Torres-Verdin, C. & Bostick, F.X., Jr, 1992. Principles of spatial surface electric field filtering in magnetotellurics: electro-magnetic array profiling (EMAP), *Geophysics,* **57,** 603–622.

Vozoff, K., 1991. The magnetotelluric method, in *Electromagnetic Methods in Applied Geophysics,* 2B, pp. 641–711, ed. Nabighian, M.N., Soc. of Explor. Geophys., Tulsa.

Wannamaker, P.E., 1999. Affordable magnetotellurics: interpretation of MT sounding profiles from natural environments, in *Three-dimensional Electromagnetics,* pp. 349–374, eds Oristaglio, M. & Spies, B., *Devel. Ser.,* no. 7, *Soc. Explor. Geophys.*, Tulsa.

Wannamaker, P.E., 2000. Comment on 'The petrologic case for a dry lower crust', by Yardley, B.D. & Valley, J.W., *J. geophys. Res.,* **105,** 6057–6064.

Wannamaker, P.E. & Doerner, W.M., 2002. Crustal structure of the Ruby Mountains and southern Carlin trend region, northeastern Nevada, from magnetotelluric data, *Ore Geol. Rev.,* **27,** 185–210.

Wannamaker, P.E. & Hohmann, G.W., 1991. *Electromagnetic Induction Studies,* US National Report to IUGG, *Rev. Geophys.*, Supplement, pp. 405–415.

Wannamaker, P.E., Stodt, J.A. & Rijo, L., 1987. A stable finite element solution for two-dimensional magnetotelluric modeling, *Geophys. J. R. astr. Soc.,* **88,** 277–296.

Wannamaker, P.E., Stodt, J.A. & Olsen, S.L., 1996. Dormant state of rifting in central west Antarctica implied by magnetotelluric profiling, *Geophys. Res. Lett.,* **23,** 2983–2987.

Wannamaker, P.E., Doerner, W.M., Stodt, J.A. & Johnston, J.M., 1997. Subdued state of tectonism of the Great Basin interior relative to its eastern margin based on deep resistivity structure, *Earth planet. Sci. Lett.,* **150,** 41–53.

Wannamaker, P.E. *et al.*, 2001. Great Basin-Colorado Plateau transition in central Utah: An interface between active extension and stable interior, in *The Geological Transition: Colorado Plateau to Basin and Range*, Proc. J. Hoover Mackin Symp., pp. 1–38, eds Erskine, M.C., Faulds, J.E., Bartley, J.M. & Rowley, P., Utah Geol. Assoc./Amer. Assoc. Petr. Geol. Guideb. 30/GB78, Cedar City, Utah, September 20–23.

Wannamaker, P.E., Jiracek, G.R., Stodt, J.A., Caldwell, T.G., Gonzalez, V.M., McKnight, J.D. & Porter, A.D., 2002. Fluid generation and pathways beneath an active compressional orogen, the New Zealand Southern Alps, inferred from magnetotelluric data, *J. geophys. Res.,* **107**(B6), ETG 6 1–20.

Wight, D.E. & Bostick, F.X., Jr, 1980. Cascade decimation—a technique for real time estimation of power spectra, *IEEE Proc. Int. Conf. Acoustic Speech and Signal Proc.,* pp. 626–629.

Winkler, H.G.F., 1979. *Petrogenesis of Metamorphic Rocks,* p. 348, Springer-Verlag, New York.

Zonge, K.L. & Hughes, L.J., 1985. Effect of electrode contact resistance on electric field measurements, in *Expanded Abstracts of 1985 Technical Programme of 55th Ann. Int. SEG Meeting,* contribution MIN 1.5, Tulsa, OK, 231–234.

APPENDIX A: MT INSTRUMENTATION OVER POLAR ICE SHEETS

A block diagram of our MT system as used at the South Pole is shown in Fig. A1(a). Control of a pair of sensor sites for synchronized data acquisition is carried out over digital radio telemetry by an operator at a convenient recording location (truck on land, towed hut in Antarctica). Low-power, embedded controllers in the receivers at the sensor sites implement remote operator commands for local hardware setup, sample timing, and two-way communication. Pre-amplified signals from the **E**-receiver and **H**-junction boxes are fed directly to the system receiver for secondary signal conditioning and

digitization, followed by telemetry to the recording location where near real-time data processing can be performed. Magnetic fields were measured using high-moment induction coils (EMI Inc.) and presented no major difficulty relative to land operation. However, specialized instrumentation is needed to acquire electric field measurements accurately in the high impedance environment presented by the firn of the polar ice cap. Previous experience in Antarctica by others with large-scale DC resistivity surveying suggested that we should design for contacts up to 10 Mohm (C. Bentley, Pers. comm.).

When contact impedances reach several Mohm, the distributed capacitance of the bipole wires requires modifications beyond
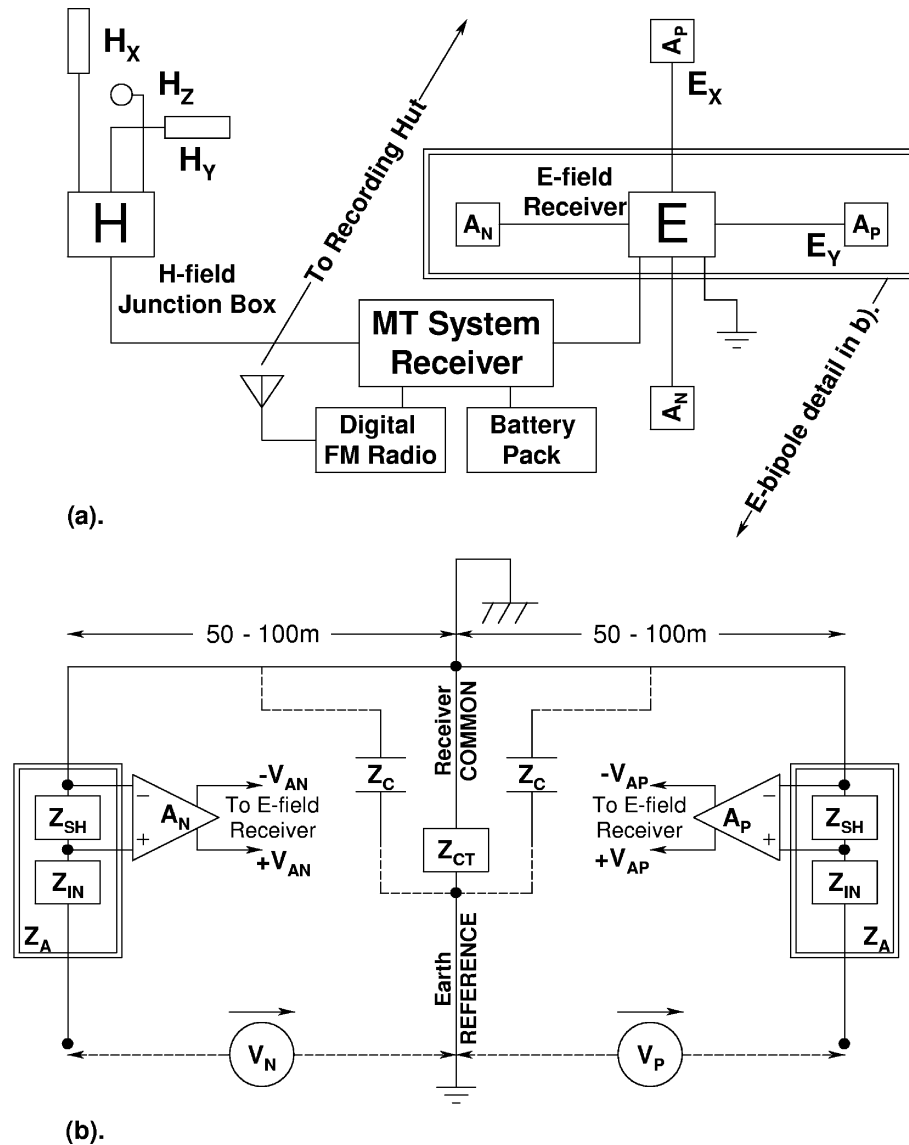

Figure A1. (a), Block diagram of MT system elements at a measurement site. **H**-field measurements are obtained using induction coils with integrated pre-amplifiers which are powered from the **H**-junction box. **E**-bipole electrodes are buffered by pre-amplifiers, A_P and A_N, which deliver half-bipole voltage measurements to a centrally located **E**-field receiver to be combined differentially before delivery to the system receiver. The double box around the E_y bipole refers to the measurement details shown in Fig. A1(b). Data acquisition is controlled via radio telemetry; (b), Simplified network model of an **E**-bipole measurement. It consists of half-bipole voltages V_N and V_P, and equivalent impedances Z_A of the electrode contact and pre-amplifier connections. Pre-amplifier inputs are connected across Z_{SH} as shown, and the outputs are driven differentially over twisted-pair wires to the **E**-field receiver. Z_{IN} is predominantly the electrode contact impedance for values large compared with the series impedance of input circuitry. The impedance Z_C represents the distributed parasitic wire-earth capacitance of the Receiver Common reference wires. Receiver Common is connected to an Earth Reference point at the centre of the bipole array through an electrode with contact impedance Z_{CT}. Wire resistance can be neglected.

simply increasing the shunt input impedance of a typical **E**-field receiver, because the capacitance and the contact impedance interact to cause attenuation and phase shifts due to unwanted voltage dividers. In a simple model, signal voltage is modified by the complex attenuation factor $[1 + j0.5X]/[1 + jX]$, where $X = \omega R C_W L$, R is electrode contact resistance, C_W is wire capacitance per unit length, L is wire length, and ω is angular frequency (Zonge & Hughes 1985, with correction). For plausible values $R = 2$ Mohm and $C_W L = 1$ nf, the (magnitude, phase) is $(0.735, -19.3°)$ at 100 Hz and $(0.999, -1.1°)$ at 3 Hz. Moreover, proximal environmental noise couples to the receiver input through a series impedance $Z_W = 1/j\omega\, C_W L$ representing the wire capacitance, and may contaminate the signal if the condition $R \ll |Z_W|$ is violated. Note that at 100 Hz, $|Z_W| \cong 1.6$ Mohm when $C_W L = 1$ nf.

Our **E**-field measurements were carried out differentially, using a 'plus' electrode array with a central common mode reference electrode, as illustrated in Figs A1(a) and (b). Total bipole lengths were 100–200 m. For robust and electrochemically stable operation in this cold environment, we used 18×24 inch expanded metal titanium sheets, buried vertically in the firn, as electrodes. Pre-amplifiers (A_P, A_N) were utilized at the positive (P) and negative (N) electrodes to isolate the high-impedance contact and thereby minimize complex voltage dividers and capacitive noise coupling. We implemented an *in situ* calibration scheme described below to quantify remaining voltage divider effects. Bipole lines to the preamps were not single wires as in land surveys, but were standard unshielded eight-conductor network cables. These carried bipolar DC power, a power return (current carrying) and a receiver common reference (current-free), differential signal, and differential calibration/control, configured in four twisted pairs as listed.

Fig. A1(b) shows a simplified network model of our **E**-field bipole measurement system. The electrode and pre-amplifier circuitry of each half-bipole are represented as an impedance Z_A, assumed equal for all half-bipoles. The impedance Z_C, of the distributed parasitic wire-earth capacitance of the receiver common reference wires (analogous to Z_W above), has no effect on the measurement of V_N and V_P, but does affect our *in situ* calibration as will be shown. Standard circuit analysis and equivalence concepts (Edminister 1965) have been used to reduce our actual circuit topology to that of Fig. A1(b). Further details and more general circuit models can be provided (contact JAS).

In Fig. A1(b), Z_A is a series combination of two impedances, Z_{IN} and Z_{SH}. Z_{IN}, a combination of the electrode contact impedance Z_{CT} and input circuitry impedance, acts in series with the '+' input of a pre-amplifier, and the pre-amp is connected across a shunt impedance Z_{SH}. The pre-amp senses a voltage V_{PR} that is amplified and delivered differentially to the **E**-field receiver at the centre of the array. Delivery of a balanced differential signal over a twisted pair of wires minimizes dielectric leakage currents across their distributed parasitic wire-earth capacitance by minimizing the effective average voltage across the capacitance. Z_{SH} is equivalently a parallel RC circuit element. The capacitive component of Z_{SH} includes 60 pf due to the connection from an electrode to its pre-amp '+' input using a 0.6 m coaxial cable (100 pf/m) with its shield connected to pre-amp common. Laboratory measurements of the total effective capacitance of Z_{SH}, including the coaxial cable connection, averaged ~120 pf and varied less than 3 per cent between amplifiers. About 40 pf of this value is parasitic, due to the physical layout of the circuit board or non-ideal performance of circuit components. With $C = 120$ pf, the equivalent impedance of Z_{SH} at frequency f is

$$Z_{SH} = 909.1\,\text{Mohm}/[1 + j0.6854\,f].$$

The DC impedance of Z_{SH}, ~909 Mohm, is a design tradeoff to provide stable open-circuit operation and to allow appropriate circuitry to protect sensitive amplifier inputs for robust field operations. At the **E**-field receiver, the half-bipole voltages are received, combined into a bipole measurement, and delivered to the MT system receiver through galvanic isolation amplifiers for further system processing.

Together, Z_{IN} and Z_{SH} create a voltage divider at the pre-amplifier inputs, i.e. $V_{P,N}$ is developed across Z_A, while V_{PR} is developed across Z_{SH}. Therefore, V_{PR} is essentially a low-pass filtered version of the desired voltage, so that $V_{P,N}$ must be recovered from V_{PR} through

$$V_{P,N} = V_{PR}[1 + Z_{IN}/Z_{SH}].$$

Anticipating that Z_{IN} could be significant compared with Z_{SH}, a calibration procedure was implemented to estimate Z_{IN} *in situ*. This was done by delivering a calibration signal V_{CAL} through a known resistor R_{CAL} to the '+' input of each electrode pre-amplifier in turn, and observing the complex voltage ratio $Q = V_{PR}/V_{CAL}$. From Fig. A1(b), note that a network consisting of both x and y **E**-field bipoles is actually driven by V_{CAL} due to their interconnection across Z_{CT}. Considering all the impedance elements of this network, circuit analysis yields

$$[Z_{IN} + (Z_{CT}||Z)] \cong R_{CAL} * Q/[1 - Q(1 + R_{CAL}/Z_{SH})],$$

where $Z = Z_C/4||Z_A/3$, and the notation $A\,||B$ indicates the parallel combination of A and B. This approximation is valid when $V_{P,N} \ll V_{CAL}[Z_{IN}/\,R_{CAL}]$.

When $|Z_{CT}| \ll |Z|$, the left-hand side of the equation is essentially $[Z_{IN} + Z_{CT}]$. Z_{IN} is approximated well by Z_{CT} when Z_{IN} is large enough to necessitate calibration, so Z_{IN} and Z_{CT} are estimated by halving the calculation on the right-hand side. Best stability is achieved when $R_{CAL} \cong 2|Z_{CT}|$, so $|Q| \cong 0.5$. However, note that $|Z|$ decreases as frequency increases. When the condition $|Z_{CT}| \ll |Z|$ is violated, $|Z_{IN}|$ and $|Z_{CT}|$ will be underestimated, as much as a factor of two when $|Z| \ll |Z_{CT}|$. Again for a wire capacitance of 1 nf, $|Z_C/4| \cong 400$ Kohm at 100 Hz, and because $|Z_A/3| > |Z_{SH}/3| \cong 4.43$ Mohm, $|Z|$ is slightly $<|Z_C/4|$.

To our pleasant surprise, low-frequency (~DC) individual electrode contact impedances at CWA were 0.2–0.25 Mohm, giving rise to voltage divider effects no greater than the data errors at the shortest periods (0.01 s). However, average temperatures at the South Pole were ~30 °C less than at CWA. Shabtaie & Bentley (1995) specify an Arrhenius dependence for firn resistivity that translates to approximately a factor of two increase per 10 °C decrease, suggesting contact impedances could approach 2 Mohm at the South Pole. Individual DC electrode contact impedances measured *in situ* at the South Pole lay in the 0.75–1.25 Mohm range. We noted a trend towards the lower values as our survey progressed, and speculate that this was at least partially due to near surface warming as the summer season progressed. Low-frequency *in situ* measurements of Z_{CT} from our MT system were generally consistent with simple measurements of DC resistance between electrode pairs using a Fluke 87 multimeter.

Our calibration methodology gave stable estimates of $|Z_{CT}|$ *in situ*, but unfortunately did not produce stable estimates of the phase of Z_{CT}. Our experience at the South Pole indicates that V_{CAL} did not always obey the condition $V_{P,N} \ll V_{CAL}[Z_{IN}/R_{CAL}]$ due to competing MT or wind-induced signals, often resulting in noisy calibration data. Our design value of $R_{CAL} = 10$ Mohm could be lowered advantageously here, but V_{CAL} cannot be increased due to current system limitations. Nor can calibration data currently be acquired at sufficiently high frequencies to fully characterize the complex

behaviour of Z_{CT}, due both to current system limitations on the maximum frequency of V_{CAL} and to the likelihood that the condition $|Z_{CT}| \ll |Z|$ is violated as frequency increases. We observed some relaxation behaviour where computed values of $|Z_{CT}|$ decreased by a factor of >2 as periods decreased from 5 to 0.02 s. This may be due in part to invalid assumption of $|Z_{CT}| \ll |Z|$, or also to a complex electrode impedance including the intrinsic capacitance of the metal electrodes buried in the dielectric firn (Reynolds 1985). Hence, complete characterization of contact effects requires a new design. These corrections would be especially important where polar ice is thin such that information concerning subice resistivity structure lies in the high-frequency data, or in considerably colder polar areas with higher resistivity firn such as around Lake Vostok or Gamburtsev Mountains.

We can estimate a maximum phase correction for our data at 0.01 s by combining the *in situ* measurements of $|Z_{IN}|$ at low frequency with the known behaviour of Z_{SH}. At 0.01 s, $|Z_{SH}| \cong 13.3$ Mohm, and the phase of Z_{SH} approaches $-90°$. With the largest observed low-frequency value of $|Z_{IN}|$ at 1.25 Mohm, we find $|Z_{IN}/Z_{SH}| \cong 0.0943$ at 0.01 s. Using 1.25 Mohm and varying the phase of Z_{IN}, a corresponding maximum value of $5.4°$ is obtained for the phase of $V_{P,N}/V_{PR}$.

Nevertheless, MT impedance phase contamination greater than $5–6°$ at the shortest periods appears to exist in our data (Figs 3 and 8). Phase values are $>85°$ at 0.1 s but fall to $75–80°$ at the shortest periods. Calculations show that with resistive ice values (e.g. $\sim$300 000 ohm m), impedance phase values should remain near $90°$ at 0.01 s. A prime suspect to cause the remaining phase rollover is calibration error due to temperature variation of system circuit components, which is most likely to occur near the cut-off frequencies of system filters. We believe our system is well calibrated, but

at room temperature. Temperature-related calibration variations in similar subcircuits of the **E**-field and **H**-field channels of our system receiver should largely cancel when computing impedance phases, and the differential **E**-field receiver is a broad-band design. However, the coil pre-amplifiers contain a 3-pole filter with a cut-off at $\sim$500 Hz and the proximity to our shortest measurement periods raises suspicions regarding the stability of the coil calibrations, because they are being operated at approximately -50 °C, $\sim$70 °C colder than when calibrated. Fortunately, the phase contamination issue is restricted to high frequencies in the South Pole survey and does not affect the data germane to the subice resistivity inversion structure and its geological interpretation.

APPENDIX B: WIND-INDUCED E-FIELD NOISE AT THE SOUTH POLE

Survey productivity and data quality at the South Pole were compromised primarily because of adverse weather conditions creating noise in the **E**-field measurement at the longer periods, especially 10–100 s. Site SPLE03 in Fig. 3 is, in fact, our best site when we were lucky to have good signal during quiet weather conditions. The noise is voltage variations in the surface ice observed to be induced during conditions of blowing, patchy ice fog and saltating ice crystals (winds $\gtrsim$ 12 knots). The noise was not due to wind-induced motion of the bipole wires because these became locked into the snow shortly after installation by blowing ice particles. Wind was not a serious problem in the magnetic fields which were generally of high signal/noise.

A manifestation of this problem on the raw **E**-field traces is given in Fig. B1. Here we see $\sim$8 min of simultaneous records of electric
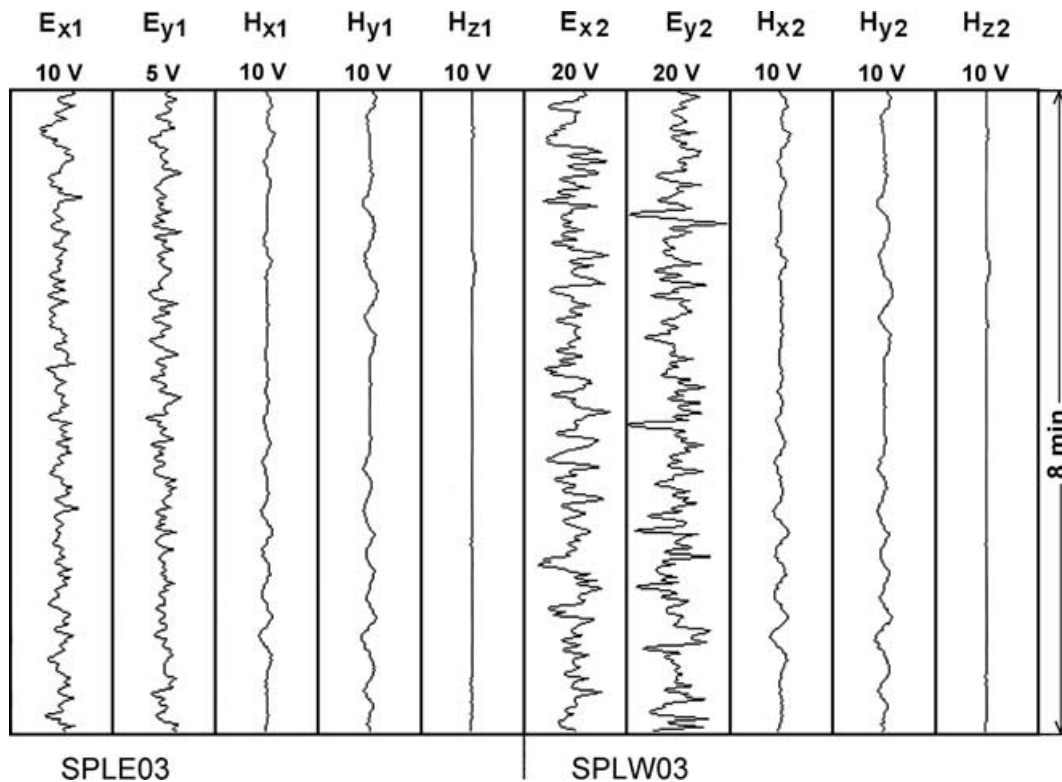

Figure B1. Simultaneous recordings of electric fields at sites SPLE03 (left-hand side) and SPLW03 (right-hand side) in the long period signal range. Plotting conventions are as in Fig. 2. Wind noise at the two sites is characteristically uncorrelated across channels and across sites; in this example it is stronger at SPLW03 than SPLE03.
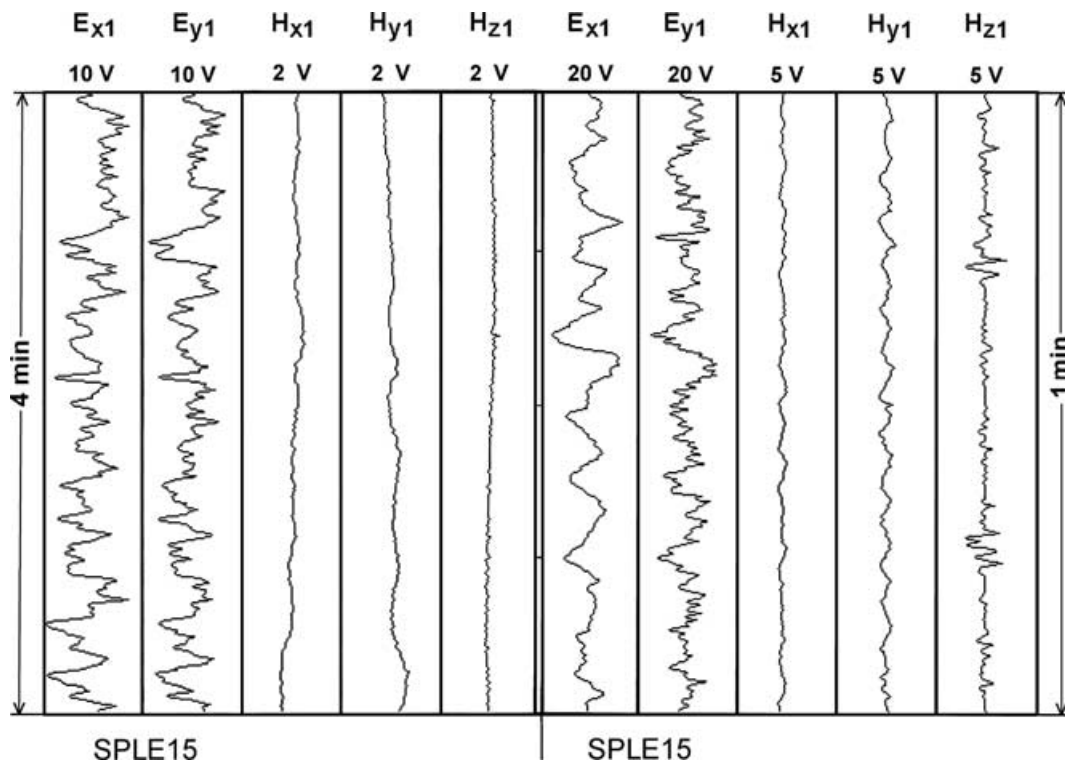
Figure B2. Recordings of electric fields on parallel bipoles of grid northeasternmost site SPLE15 as a test of electronics fidelity and wind noise. Plotting conventions are as in Fig. 2. The recordings in the left-hand panel and the right-hand panel were not taken synchronously and represent two separate experimental recordings.

and magnetic fields at SPLE03 and companion site SPLW03. The hardware gains in this run were identical to those of Fig. 3 but the MT signal strengths were substantially less at this time as indicated by the expanded strip chart scale for the **H**-fields. Hence, the **E**-field strength relative to **H** must be much greater than in Fig. 3. More important, there is a complete lack of correlation of the **E**-fields with the **H**-fields, or between E_x and E_y at each site, or between the **E**-fields across the two sites. There were only 2 or 3 instances in the whole survey during sustained wind gusts where visual correlations between E_x and E_y at a site were convincing. Ordinary coherences computed between E_x and E_y at a site were typically only 0.02–0.04.

That the spurious **E**-field noise exists in the ice was demonstrated by parallel **E**-line tests in windy conditions (Fig. B2). The first took place with the two bipole channels and their electrode preamps connected to the same buried titanium electrode. The **E**-field traces show excellent correlation with each other but not with the **H**-field, verifying the fidelity of our electronics while showing that these **E** variations are not MT signal. The second test occurred with the bipoles and preamps connected to separate but close (∼3 m) electrodes. In this case, the **E**-field traces show visible correlations especially in the relatively longer period variations, but the **E**-field trace to the right-hand side shows added high-frequency character that is additional noise. We observed that swirling ice particle wisps were unique around each electrode implantation, and attribute the difference in **E**-field traces in Fig. B2 to this condition. It suggests that care in levelling the electrode sites could reduce noise, but we did not assess that in this test. During this test, wind was strong enough to produce intermittent noise spikes in Hz, which are uncorrelated with **E** noise due to sensor separations of ∼100 m.

Above a typical wind speed of 10–15 knots, movement and suspension of ice crystals in the air is observed. Volumes of suspended

ice crystals (clouds) tend to acquire surface electrical charge through diverse possible mechanisms (MacGorman & Rust 1998). The sign, magnitude and distribution of net charge may be highly variable, although ice crystals should tend to acquire a net negative charge through thermoelectric effects when the wind is warmer than the surface (expected for polar summer) (Schmidt & Dent 1993). For our purposes, however, the exact distribution is not critical since any charge distribution is a superposition of elementary volumes (e.g. Stratton 1941). We propose that such charge distributions are the cause of the measured **E**-field noise because of the temporal correspondence of their appearance with the noise.

For simplicity and without loss of generality, consider a spherical distribution of electric charge over the Earth's surface. Such a volume produces a zero-mean, antisymmetric **E**-field distribution along the surface (Stratton 1941). The characteristic wavelength of the field variation is proportional to the effective diameter, or height, of the charge sphere. For a given charge density, small charge clouds spanned by an MT bipole have relatively little effect on the total measured **E**-field because the bipole responds to the average **E**-field (voltage difference) along its length (200 m in our case) and the charge anomalies are zero-mean. Small but dense and persistent charge clouds near the bipole ends during exceptionally windy times may contribute noise as exemplified in Fig. B2. However, we argue as follows that it is the large or elevated charge clouds, the anomaly widths of which compare to a bipole span, which cause the main **E**-field noise problem encountered as shown in Fig. B1.

The period range of MT data which is corrupted by noise will depend upon the speed with which the antisymmetric charge anomaly moves along the bipole. At a speed of 15 knots (∼8 m s^{-1}), a 200 m bipole will be traversed in approximately 25 s. Charge distributions creating antisymmetric **E**-field anomalies comparable to the bipole

length will induce positive/negative temporal swings in the measured **E**-field over a similar period. Larger charge distributions of longer spatial wavelength may affect longer MT data periods for a given wind speed. If **E**-field noise variations of all wavelengths have equal amplitudes, MT data periods longer than a certain value ($\gtrsim$10s in our case) should all be equally corrupted. Curiously, our data suggest that the problem diminished somewhat for $T > 200$–300 s, based on somewhat reduced impedance error bars, implying that the wind-generated noise may be somewhat band-limited spatially and hence in period.

This is supported by the observation that the **E**-field noise almost invariably is not correlated across x- and y-bipoles of a single site (Fig. B1), let alone across different sites. It implies that the causative charge volumes are not coherent over large distances or, equivalently, each volume has a short time duration before disintegrating and being replaced by another. It strongly suggests that the wind noise problem, at least for moderate wind velocities, could be overcome by substantially increasing the **E**-field bipole length and hence the signal/noise. Particle noise from cloud wavelengths much greater than the bipole should also be suppressed by the common mode rejection of our electronics, which could in part explain data improvement at the longest periods. Parallel **E**-line tests with greatly varying line length could help quantify spatial wavelengths of ice particle wind noise and its influence on MT recording.